An intracontinental orogen exhumed by basement-slice imbrication in the Longmenshan Thrust Belt of the Eastern Tibetan Plateau

Zhenhua Xue, Wei Lin, Yang Chu, Michel Faure, Yan Chen, Wenbin Ji, Huaning Qiu

An intracontinental orogen exhumed by basement-slice-imbrication in the Longmenshan Thrust Belt of the Eastern Tibetan Plateau

Zhenhua Xue[1,2,3], Wei Lin[2, 4], Yang Chu[2, 4], Michel Faure[3], Yan Chen[3], Wenbin Ji[5], Huaning Qiu[6]

[1] School of Earth Sciences, China University of Geosciences, Wuhan 430074, China

[2] State Key Laboratory of Lithospheric Evolution, Institute of Geology and Geophysics, Chinese Academy of Sciences, Beijing 100029, China

[3] Univ. Orléans, CNRS, BRGM, ISTO, UMR 7327, F–45071, Orléans, France

[4] University of Chinese Academy of Sciences, Beijing 100049, China

[5] Department of Geology, Northwest University, Xi'an 710069, China

[6] Key Laboratory of Tectonics and Petroleum Resources (China University of Geosciences), Ministry of Education, Wuhan 430074, China

Corresponding author: Wei Lin (linwei@mail.iggcas.ac.cn)

Key Points

1. The double-vergent structure of the Longmenshan belt was established during the late Triassic intracontinental underthrusting
2. Boundary faults of the NW-normal faulting and SE-thrusting facilitated the SE-ward basement-slice imbrication
3. The episodic basement-slice imbrication exhumed the early Mesozoic metamorphic rocks

Abstract The Longmenshan Thrust Belt (LMTB) in the Eastern Tibet resulted from a Mesozoic orogeny and Cenozoic reworking. It is generally believed that the Cenozoic tectonics along the LMTB are mostly inherited from the Mesozoic one. Reconstruct the Mesozoic tectonics of the LMTB is therefore important for understanding its evolutionary history. On the basis of detailed structural analysis, we recognized a Main Central Boundary that divides the LMTB into a Southeastern Zone and a Northwestern Zone. Both zones underwent a main D_1 event characterized by the D_{1E} top-to-the-SE thrusting in the Southeastern Zone and the D_{1W} top-to-the-NW/N thrusting in the Northwestern Zone. In the Southeastern Zone, a D_2 top-to-the-NW/N normal faulting

that cuts the D_{1E} structures is developed along the NW boundary of the basement complexes. Newly obtained and previous geochronological data indicate that the D_{1E} and D_{1W} event occurred synchronously at *ca*. 224–219 Ma, and the D_2 top-to-the-NW/N normal faulting was episodically activated at *ca*. 166–160 Ma, 141–120 Ma, 81–47 Ma and 27–25 Ma. Episodically and synchronously activated top-to-the-NW normal faulting and top-to-the-SE thrusting along the northwest and southeast boundary of the basement complexes, respectively, let us propose that the basement-slices were episodically imbricated to the SE during the late Jurassic–early Cretaceous and late Cretaceous–earliest Paleocene. The D_1 amphibolite-facies metamorphic rocks above the basement complexes recorded fast exhumation during the late Jurassic–early Cretaceous. We propose that the early Mesozoic northwestward basement underthrusting along a crustal "weak zone" was responsible for the D_1 double-vergent thrusting and amphibolite-facies metamorphism. Subsequent basement-slice imbrications reworked the LMTB and exhumed the amphibolite-facies rocks. Our results highlight the importance of basement underthrusting and imbrication in the formation and reworking of the intracontinental Longmenshan Thrust Belt in the Eastern Tibet.

1. Introduction

The Longmenshan Thrust Belt (LMTB; Figure 1a), at the eastern margin of the Tibetan Plateau, has attracted attentions of geologists due to the paradox between low convergence rate (Zhang et al., 2004; Shen et al., 2009) and extremely high topographic gradient (Clark and Royden, 2000; Royden et al., 2008) as well as intense seismic activities (e.g., 2008 Wenchuan Mw 7.9 earthquake, 2013 Lushan Mw 7.0 earthquake, and 2017 Jiuzhaigou Mw 7.0 earthquake). This paradox has spawned a vigorous debate regarding the roles of upper crustal faulting (Hubbard and Shaw, 2009) and lower crust channel flow (Royden et al., 2008) in building and maintaining such a high Tibetan Plateau margin. However, both models attribute shortening and crustal thickening of the LMTB to the late Cenozoic evolution, and underestimate the importance of widely recognized Mesozoic tectonics along the LMTB (Xu et al., 1992; Burchfiel et al., 1995; Worley and Wilson, 1996). Furthermore, it has been reached a consensus that the LMTB is mainly inherited from the Mesozoic tectonic framework (Burchfiel et al.,

1995; Meng et al., 2005). Elucidating the Mesozoic tectonics of the LMTB and its adjacent areas is therefore crucial to understand the tectonic evolution of the LMTB.

The prominent deformation recorded in the LMTB and adjacent areas is indicated by observations including: 1) the peripheral foreland basin formed due to the southeastward thrusting and loading of the LMTB (Chen et al., 1994; Li et al., 2003); 2) the early Jurassic rocks unconformable overly extensively folded late Triassic rocks (BGMRSP, 1991; Xu et al., 1992; Burchfiel et al., 1995); 3) the pervasive orogen-parallel klippen and nappe belt sitting on the foot hills of the Longmen Mountains are believed related to the regional top-to-the-SE thrusting (Figure 2); 4) the consistent top-to-the-SE thrusting indicated by different indicators at various scales (Xu et al., 1992; Burchfiel et al., 1995; Chen et al., 1995; Chen and Wilson, 1996; Jia et al., 2006; Yan et al., 2011; Yan et al., 2018); 5) the pervasive upright folding in the adjacent Songpan–Ganzi Terrane was thought synchronous to the early Mesozoic deformation of the LMTB (Burchfiel et al., 1995; Chen et al., 1995; Harrowfield and Wilson, 2005). This prominent deformation event was constrained to *ca.* 234–200 Ma by basin tectonics, timing of the top-to-the-SE/SSE shearing and syntectonic metamorphism, which indicated an early Mesozoic orogeny of the LMTB (Chen et al., 1994; Li et al., 2003; Yan et al., 2011; Zheng et al., 2014; Xue et al., 2016; Zheng et al., 2016; Airaghi et al., 2018a; Airaghi et al., 2018b; Yan et al., 2018).

The early Mesozoic tectonic evolutionary mechanism accounting for the above observations, however, is still in dispute. Sengör (1984) and Luo (1991) suggested that the LMTB is an early Mesozoic intracontinental subduction zone accommodating multi-stage crustal shortening. Then, Xu et al. (1992) proposed a bivergent subduction model in which the Songpan–Ganzi Terrane sedimentary cover has been "pushed" to the southeast on top of the Yangtze Block due to the bivergent subduction along the Anymaqen and Jinshajiang Suture Zones. The current models suggested that the Songpan–Ganzi sedimentary cover were overthrust southwards on the Yangtze Block along a decollement in response to the closure of the Paleotethys (Mattauer et al., 1992; Calassou, 1994; Dirks et al., 1994; Chen and Wilson, 1996; Worley and Wilson, 1996; Roger et al., 2004; Harrowfield and Wilson, 2005; de Sigoyer et al., 2014; Yan et al., 2018).

Apart from the early Mesozoic top-to-the-SE/SSE thrusting along the LMTB, an increasing number of studies proposed a top-to-the-NW normal faulting that developed

along the NW boundary of the orogen-parallel and stripped Neoproterozoic complexes (Figure 1b)(Xu et al., 2008; Zhou et al., 2008; Tian et al., 2016; Billerot et al., 2017; Xue et al., 2017; Airaghi et al., 2018b). However, timing and significance of the top-to-the-NW normal faulting are in dispute that have resulted in several different models, such as: 1) mid-Jurassic to early Paleogene (173–160 Ma and 81–47 Ma) post orogenic extension (comparing to the early Mesozoic orogeny)(Zhou et al., 2008), 2) early Cretaceous (~120 Ma) crustal-scale wedge extrusion (Xu et al., 2008), 3) episodic eastward basement-slice-imbrication during the late Jurassic–early Cretaceous and late Cretaceous–Earliest Paleogene (Billerot et al., 2017; Xue et al., 2017), and, 4) formation of a late Cretaceous–earliest Paleogene crustal scale duplex (Tian et al., 2016). Based on the above compilation, most previous works have proposed that the top-to-the-NW normal faulting occurred in the late Mesozoic.

Major questions therefore remain unsolved: 1) Considering previous early Mesozoic tectonic models of the LMTB, whether did the significant shortening recorded in the LMTB correspond to the imbricated thrust system during the Paleotethys' closure, or to the intracontinental underthrusting along the Longmenshan belt? 2) What is the tectonic significance of the top-to-the-NW normal faulting (mostly late Mesozoic) and emplacement of the Neoproterozoic complexes? Therefore, an overall accurate reconstruction of the Mesozoic tectonics of the LMTB and its adjacent areas, especially its detailed structural analysis and timing, are of great importance.

This study presents detailed field investigations focusing on structural geometry and kinematic reconstruction, and geochronological constraints including zircon U–Pb dating of synkinematic plutonic rocks and $^{40}Ar/^{39}Ar$ dating on the synmetamorphic micas of the LMTB. In conjunction with previous published geochronological and metamorphic data, a new geodynamic model was proposed to interpret the Mesozoic tectonic evolutionary history of the LMTB.

2. Geological Setting

At the eastern margin of the Tibetan Plateau, the LMTB separates the intensely folded and metamorphosed (Greenschist facies grade) Songpan–Ganzi Terrane to the NW, and the weakly/undeformed Sichuan Basin to the SE (Figure 1a). The triangle-shaped Songpan–Ganzi Terrane is separated from the western Qinling–Dabie Orogenic

Belt to the north by the East Kunlun–Anymaqen Suture Zone, from the Qiangtang Block to the southwest by the Jinshajiang Suture Zone (Figure 1a).

2.1 Songpan–Ganzi Terrane

The Songpan–Ganzi Terrane mainly comprises ~5–15 km-thick intensely folded late Triassic turbidites (Calassou, 1994; Harrowfield and Wilson, 2005; Zhang et al., 2006c; Zhang et al., 2008; Yin, 2015). The provenance of the turbidites includes the Kunlun Mountains, North China Block, South China Block and southwest Qinling Orogenic Belt (Yin and Nie, 1993; Enkelmann et al., 2007; Weislogel et al., 2010). Voluminous felsic plutons intruded the Songpan–Ganzi Terrane at *ca.* 226–205 Ma, dominantly derived from partial melting of the Neoproterozoic basement and sedimentary cover of the Songpan–Ganzi Terrane, with negligible amounts of mantle material (Figure 1b)(Roger et al., 2004; Hu et al., 2005; Zhang et al., 2006b; Zhang et al., 2007; de Sigoyer et al., 2014). Both geophysical and geological data indicate a continental crust of Yangtze Block affinity underlying the eastern Songpan–Ganzi Terrane (Roger et al., 2004; Hu et al., 2005; Zhang et al., 2009; Weislogel et al., 2010; Zhang et al., 2010; Guo et al., 2013).

2.2 Sichuan Basin of the Yangtze Block

The Sichuan Basin, located in the Yangtze Block of northwest South China Block (Figure 1a), preserves a Paleoproterozoic to Neoproterozoic basement overlain by Neoproterozoic to Cenozoic sedimentary sequences. Silurian–Devonian abyssal deposits and radiolarian chert suggested a long period of rifting during the Silurian to Devonian ages along the western part of the Yangtze Block (Long, 1991; Luo, 1991; Chang, 2000; Li, 2009). This rift was revealed by high-resolution seismic reflection profile as well (Jia et al., 2006). During middle–late Triassic ages, coeval with the southeastward thrusting and loading of the LMTB, the western Sichuan Basin began subsiding flexurally and evolved into an epicontinental foreland basin (Figure 2). Thrust sheets were transported to the southeast synchronously and intensely folded at the end of the late Triassic (Chen et al., 1994; Chen and Wilson, 1996; Li et al., 2013c). The continuous sedimentation of the middle Jurassic–upper Cretaceous deposits implies a pronounced subsidence at the western Sichuan foreland basin during this period (Burchfiel et al., 1995; Chen et al., 1995). Episodic SE-ward thrusting and loading of the LMTB were indicated by the wedge-shaped megasequences of the western Sichuan foreland basin, namely, in late Triassic–early Jurassic, late Jurassic–

early Cretaceous and late Cretaceous–earliest Paleocene (Xu et al., 2008; Li et al., 2013c; Tian et al., 2016).

2.3 The LMTB

The NE-striking LMTB merges into the western Qinling Orogenic Belt to the northeast and is truncated by the Xianshuihe Fault to the southwest (Figure 1a).

2.3.1 Major faults of the LMTB

The regional tectonic architecture of the LMTB is defined by four major NE–SW striking faults, namely from the southeast to the northwest, the Anxian–Guanxian Fault (T_1 in Figure 1b), the Yingxiu–Beichuan Fault (T_2 in Figure 1b), the Wenchuan–Maoxian Fault (T_3 in Figure 1b), and the Qingchuan–Pingwu Fault (T_4 in Figure 1b). The Anxian–Guanxian Fault dips to the northwest by 30–50° and crosscuts the late Triassic–early Jurassic rocks. Approaching northwestwards, the Yingxiu–Beichuan Fault dipping 40–60° to the NW separates the Sichuan foreland basin to the southeast from the LMTB hinterland (BGMRSP, 1991; Xu et al., 1992; Burchfiel et al., 1995). The Wenchuan–Maoxian Fault dipping 30–50° to the NW was episodically activated since *ca.* 220 Ma (Burchfiel et al., 1995; Yan et al., 2008; Zheng et al., 2016). Seismic reflection profile showed that the ENE-striking Qingchuan–Pingwu Fault dips to the NNW or SSE at variable angles (Wang et al., 2000; Jia et al., 2006; Lin et al., 2014). The northern LMTB was dissected by the Qingchuan–Pingwu Fault and incorporated to northwestward- and southeastward-thrusting that resemble a positive flower structure (Jia et al., 2006). The Wenchuan–Maoxian Fault and Qingchuan–Pingwu Fault are characterized by mylonite overprinted by breccia and gouge (Chen and Wilson, 1996; Li et al., 2013a; Li et al., 2015).

2.3.2 Basement complexes in the LMTB

The basement complexes that distributes from the NE to the SW in the LMTB are composed of Neoproterozoic meta-granites overlain by a Neoproterozoic meta-sedimentary cover, such as the Danba (DB), Kanding (KD), Wulong (WL), Baoxing (BX), Pengguan (PG), Moutuo (MT), Xuelongbao (XLB) and Jiaoziding (JZD) complexes (Figure 1b). These basement complexes share similar lithology with the Yangtze Block basement (BGMRSP, 1991). Field observations, Anisotropy of Magnetic Susceptibility (AMS) and gravity modeling have suggested that these basement complexes were strongly deformed and imbricated southeastwards as

basement-slices (Ma et al., 1996; Xu et al., 2008; Tian et al., 2016; Airaghi et al., 2017b; Billerot et al., 2017; Xue et al., 2017).

2.3.3 Metamorphism in the LMTB

Two amphibolite facies metamorphic zones have been recognized in the meta-sedimentary cover in the Wenchuan–Xuelongbao area and the Danba area (Dirks et al., 1994; Huang et al., 2003a; Zhou et al., 2008; Airaghi et al., 2018a; Airaghi et al., 2018b). Petrological studies (garnet–amphibolite–biotite thermometer, pseudosection using Perplex modeling and chlorite–white mica–quartz thermal dynamic equilibrium) constrain the peak metamorphic conditions at ~11 ± 2 kbar, ~620 ºC in the Wenchuan–Xuelongbao area (Dirks et al., 1994; Airaghi et al., 2018a) and ~5.3–8 kbar, 570–680 ºC in the Danba area (Huang et al., 2003a; Weller et al., 2013). The Wenchuan–Xuelongbao metamorphic belt reached amphibolite facies conditions at *ca*. 210–180 Ma (Airaghi et al., 2018a; Airaghi et al., 2018c) and recorded fast exhumation at *ca.* 140–120 Ma (Arne et al., 1997; Airaghi et al., 2018c). The Danba amphibolite-facies metamorphic belt reached peak conditions at *ca*. 205–180 Ma (Huang et al., 2003a; Weller et al., 2013) and initiated enhanced rapid cooling at *ca.* 168–158 Ma (Huang et al., 2003a; Zhou et al., 2008).

Apart from these two amphibolite facies metamorphic zones, late Triassic blueschists occur as lenses along the Qingchuan–Pingwu Fault, with peak metamorphic pressure attained to 5.2–6.5 kbar (Wei, 1994; Xu et al., 2020). The blueschist then have been retrograded to greenschist in a nearly isothermal decompression way (Wei, 1994).

2.3.4 Tectonic events of the LMTB

The LMTB recorded at least three phases of deformation, including (1) D_1, the late Triassic to early Jurassic regional top-to-the-SE thrusting, (2) D_2, the top-to-the-NW/N normal faulting of poorly constrained timing and tectonic significance, and (3) D_3, the Cenozoic shortening reactivation (Xu et al., 1992; Burchfiel et al., 2008; Richardson et al., 2008; Xu et al., 2008; Li et al., 2013a; Li et al., 2015; Tian et al., 2016; Xue et al., 2017). The D_1 deformation is well identified by penetrative cleavages (S_1), mineral and stretching lineation (L_1) in the Wenchuan area, and the top-to-the-SE thrust sheets and nappes over the intensely folded late Triassic sequences in the western Sichuan foreland basin (Xu et al., 1992; Burchfiel et al., 1995; Worley and Wilson, 1996; Li et al., 2003). Most parts of the Songpan–Ganzi Terrane show slow cooling rate at *ca.* 1°C/Ma since the early Mesozoic (Huang et al., 2003a; Huang et al., 2003b; Roger et al., 2011).

However, an enhanced cooling event (*ca.* 8°C/Ma) during the late Jurassic to Eocene was reported at the peripheries of the Songpan–Ganzi Terrane, especially in the Wenchuan and Danba areas (Yuan et al., 1991; Arne et al., 1997; Huang et al., 2003a). This rapid cooling event probably responded to the D_2 top-to-the-NW/N normal faulting. The belt characterized by the top-to-the-NW normal faulting developed along the northwest/north boundary of the basement complexes was entitled as the East Tibet Detachment (Wang et al., 2012b). The D_3 deformation was thought to have initiated since *ca.* 30–25 Ma that builds the present Longmen mountains of the eastern Tibetan Plateau (Clark and Royden, 2000; Kirby et al., 2002; Wang et al., 2012a).

3. Structural analysis of the LMTB

3.1 Structural subdivisions of the LMTB

The LMTB was interpreted as an allochthonous sheet thrusting southeastward upon the autochthonous western Sichuan Foreland Basin (Xu et al., 1992; Burchfiel et al., 1995; Worley and Wilson, 1996; Robert et al., 2010a). Based on structural investigations, we present revised structural subdivisions of the LMTB. Firstly, the LMTB is divided into a Southeastern Zone and a Northwestern Zone by a Main Central Boundary (see Section 3.2; Figure 3a). According to the lithology, deformation intensity, and metamorphic grade, the Southeastern Zone can be further subdivided into four subdivisions (Figure 3). They are, from the southeast to the northwest: i) the undeformed Autochthon that comprises the western part of the Sichuan Foreland Basin, ii) the Para-autochthon, transported southeastwards along the Anxian–Guanxian Fault and rests over the Autochthon, iii) the Allochthon that traveled southeastwards much further on top of the Para-autochthon, and iv) the Inner Metamorphic Core that recorded the highest metamorphic conditions (*i.e.*, amphibolite facies) among the Southeastern Zone. The four subdivisions in the Southeastern Zone are separated by the three major listric faults of the LMTB (Figure 3; see in Section 2.3.1).

i) The Autochthon, located to the southeast of the Anxian–Guanxian Fault, is mainly composed of Jurassic–Cretaceous strata and overlying Cenozoic sediments (Figures 3 and 4). The Jurassic–Cretaceous strata were deposited in circumstances of alluvial, fluvio-deltaic, and lacustrine fills, characterized by medium and coarse-grained sandstone with some conglomeratic layers at the base. Total thickness of the Jurassic–Cretaceous sequences is more than 5 km (BGMRSP, 1991). In the northern part of the

LMTB, close to Anxian and Jiangyou county, the early Jurassic and overlying Cretaceous to Cenozoic sequences are dipping to the southeast that unconformably rest on the intensively folded late Triassic rocks (Figures 2 and 4c–d)(BGMRSP, 1991).

ii) The Para-autochthon is sandwiched by the Anxian–Guanxian Fault and the Yingxiu–Beichuan Fault, with its half area covered by klippen and nappes from the Allochthon (Figure 3). The Late Triassic Xujiahe Formation dominated in this subdivision either passes up from the earliest late Triassic marine sandstone or unconformably overlies the middle Triassic limestone (Li et al., 2003; Meng et al., 2005). The Xujiahe Formation shows markable lateral variation in both thickness and sedimentary facies. Coarse-grained sediments, such as alluvial conglomerate bodies occur close to the Yingxiu–Beichuan Fault, but change into fine-grained lacustrine sediments toward to the basin interior.

iii) The Allochthon is mainly exposed between the Wenchuan–Maoxian Fault and the Yingxiu–Beichuan Fault, and also includes the klippen and nappes resting on top of the Para-autochthon (Figures 2 and 3a). Northwest to the Yingxiu–Beichuan Fault, this subdivision mainly consists of Silurian shale and greywacke with the bedding completely transposed into foliation. Greenschist-facies metamorphism is indicated by mineral assemblages of fine-grained muscovite + chlorite + quartz (Airaghi et al., 2017b; Xue et al., 2017). Metamorphic condition jumps of ~50 ºC, 3–5 kbar southeastwards across the Yingxiu–Beichuan Fault suggest that the Allochthon are more deformed and metamorphosed in a deeper structural level than the Para-autochthon (Robert et al., 2010a; Airaghi et al., 2018b). Neoproterozoic complexes including the Pengguan and Jiaoziding complexes are distributed in this subdivision. Southeast to the Yingxiu–Beichuan Fault, klippen and nappes are mainly composed of Devonian to early Triassic thick-bedded limestone and marine sandstone (Figures 2, 3 and 4a–d).

iv) The Inner Metamorphic Core comprises phyllite and micaschist that are mostly metamorphosed Silurian sediments (Figures 2 and 3). Amphibolite-facies metamorphic zone that wraps the oval-shaped Xuelongbao (XLB in Figure 2) and stripped Moutuo (MT in Figure 2) complexes records the highest-grade metamorphism within the Southeastern Zone (Dirks et al., 1994; Airaghi et al., 2017a; Airaghi et al., 2018a). Peak P–T condition attained to ~11 ± 2 kbar and ~620 ºC at the southernmost margin of the Xuelongbao complex calculated from metamorphic assemblages of biotite + garnet +

staurolite + muscovite + kyanite (Dirks et al., 1994; Airaghi et al., 2018a). Based on the enhanced metamorphic grade and deformation intensity, the Inner Metamorphic Core are therefore more deformed and metamorphosed in a deeper structural level than the Allochthon.

The Northwestern Zone includes eastern Songpan–Ganzi Terrane with Neoproterozoic sequences outcropped in the north and Paleozoic sequences outcropped in the south (Figures 2 and 3). The northern Northwestern Zone mainly consists of two Neoproterozoic Groups, namely, 1) the volcanic Bikou Group defined by mafic lavas within its lower part and ranges from mafic to intermediate–felsic within its upper portion, and 2) the Hengdan Group tectonically resting on the Bikou Group is composed of black, thin-bedded pyrite-bearing shales and interbedded thinly volcaniclastic sandstone and siltstone (Yan et al., 2003; Druschke and Wang, 2006). The southern Northwestern Zone includes Devonian Weixian Formation and the Triassic sequences. The Devonian sequences consist mainly of quartziferous phyllite to schist and interbeded quartzite. The overlying Triassic Xikang Group is dominated by thick and highly repetitious flysch sediments. Although different rock units comprising the northern and southern Northwestern Zone, it was metamorphosed under similar greenschist facies conditions (Figures 1b and 2)(Xu et al., 1992; Liu et al., 2008)

3.2 The Main Central Boundary

The Main Central Boundary serves as a major tectonic boundary separating the Northwestern Zone and the Southeastern Zone. It corresponds to the southern branch of the Qingchuan Fault (T_4 in figure 2) in the north (BGMRSP, 1991), and to a vertical cleavage zone within the Paleozoic rocks in the south (Figure 2). To the SE of the Main Central Boundary, all structural planes in the Southeastern Zone, including foliations, cleavages, and fold axial planes, are exclusively dipping to the NW. Various kinematic indicators in the Southeastern Zone suggest a consistent top-to-the-SE/S thrusting. To the NW of the Main Central Boundary, the Northwestern Zone is characterized by the SSE-dipping planar structures and associated top-to-the-NW thrusting (Figure 3).

The Qingchuan–Pingwu Fault, as the northern segment of the Main Central Boundary, is a major tectonic boundary. Seismic profiles, drill data (Jia et al., 2006) and field observations indicate that the Qingchuan–Pingwu Fault is a positive flower structure developed in a transpressional system. Microfabric study (Wang et al., 2000)

indicated that the Qingchuan–Pingwu Fault was originated from a deep-seated ductile shear zone during late Triassic and overprinted by Cenozoic brittle deformation at very least. It is the late Triassic deep-seated ductilely sheared Qingchuan–Pingwu Fault rather than the Cenozoic brittle one that separates the LMTB into the Southeastern Zone and Northwestern Zone.

The southern segment of the Main Central Boundary roughly distributes along the geological boundary between the Silurian and Devonian–Permian sequences (Figure 2). Macroscopically, this segment of Main Central Boundary shows predominant vertical cleavage and foliation within intensely deformed argillaceous limestone, graphitic pelite and thin-bedded limestone–quartz ribbon interlayers (Figures 3a and 5). Their bedding (S_0) can be distinguished by the compositional variations that is parallel to the cleavages (Figure 3a and 5b). Associated rootless folds imply significant shortening during the formation of the Main Central Boundary (Figures 3a and 5b–c). P-wave receive function and seismic reflection profiles revealed a Moho at ~36–40 km depth beneath the Sichuan Basin that gradually deepens northwestwards at ~63 km depth beneath the eastern Tibet (Guo et al., 2013). This transition occurs beneath the Wenchuan Shear Zone (corresponding to Inner Metamorphic Core) over a horizontal distance of fewer than 30 km (Robert et al., 2010b; Zhang et al., 2010; Guo et al., 2013). Geophysical profiles, therefore, support the statement that the southern Main Central Boundary, as the northwest boundary of the Inner Metamorphic Core, serves as a major tectonic boundary.

3.3 The main deformation (D_1)

The D_1 main deformation is defined by a NW–SE striking stretching lineation recognized in both the Southeastern and Northwestern zones which is separated by the Main Central Boundary (Figure 2). Kinematic indicators indicate a top-to-the-SE thrusting and a top-to-the-N/NW thrusting in the Southeastern and the Northwestern zones, respectively. Since there is no evidence of superposition between these two senses of shear, it is difficult to precisely define the relative timing of these opposite shearing events. Nevertheless, to clarify the presentation of the deformation events, in the following, we distinguish D_{1E}, the top-to-the-SE thrusting in the Southeastern Zone, and D_{1W}, the top-to-the-NW/N thrusting in the Northwestern Zone, respectively.

3.3.1 Top-to-the-SE thrusting in the Southeastern Zone (D_{1E})

The top-to-the-SE shearing and thrusting are widespread in the Southeastern Zone at variable scales, except that the Autochthon merely recorded long-wavelength fold and monoclines toward the interior of the Sichuan Basin (Figure 4). The D_{1E} top-to-the-SE thrusting is most developed in the Inner Metamorphic Core and generally attenuated southeastwards.

The Inner Metamorphic Core was ductilely deformed showing predominant NW-dipping foliation (S_1) at varied angles between 60–90°. Specifically, the foliation gradually steepens when approaching the Main Central Boundary, and eventually presents in a vertical attitude (Figures 2–4). This changing trend of foliation implies that the deformation intensified toward the Main Central Boundary. Foliations mostly consist of an alternation of biotite-white mica-rich and light-colored, pelitic interlayers (Figures 3a and 6a–b). Along the transect from Wenchuan county to Xuecheng town, an NW-plunging mineral and stretching lineation (L_1) defined by aligned newly formed biotite, white mica, elongated quartz aggregates, or iron-oxide pods are well developed (Figures 3a and 6a). Kinematic indicators document a consistent top-to-the-SE thrusting in the Inner Metamorphic Core. Such as asymmetric pyrite pressure shadow in mica-schist (Figures 3a and 6b) and sigma-shaped feldspar porphyroclasts in paragneiss (Figures 3a and 6c) both show top-to-the-SE thrusting. Photomicrographs (perpendicular to the foliation and parallel to the lineation) show that newly formed white mica oriented as compaction plane (S) and shear plane (C), both of which composes an S-C fabric documenting a consistent top-to-the-SE thrusting (Figures 3a and 6d).

In the Allochthon, the Neoproterozoic complexes such as the Pengguan and Jiaoziding complexes, mostly show brittle deformation characterized by subhorizontal joints. Inside the Pengguan complex, several NE–SW trending ductile shear zones dissected and thrust the granitic rocks to the southeast (Airaghi et al., 2017b; Xue et al., 2017). Upon the granitic rocks, the Neoproterozoic Huangshuihe Group recorded extensive shearing and sigmoid pelitic lens incorporated to the top-to-the-SE thrusting (Figures 3a and 6e). Structural planes including axial planar cleavages and spaced cleavages dip to the northwest at angles of 30–65° (Figures 2–4). Fine-grained white mica and chlorite are developed on these structural planes demonstrating a greenschist facies grade of deformation. Sigma-shaped sandy lens in the Silurian pelitic schist indicate a top-to-the-SE thrusting as well (Figures 3a and 6f).

As part of the Allochthon, most of the klippen are synclines overturned to the SE, with SE-ward reverse fault which dissected the thick Devonian limestone at the rear of the klippe (Figures 2 and 6g), and show a consistent top-to-the-SE thrusting (BGMRSP, 1991).

In the Para-autochthon, the late Triassic Xujiahe sandstone is intensively folded as indicated by the NE-SW trending π-circle-projected axis of bedding (Figures 3b-d). In the south part, multi π circle-Axis exist roughly trending NE-SW, implying multiphase of shearing and thrusting. Folds are mostly overturned to the SE indicating a top-to-the-SE thrusting (Figure 2). Axial planar cleavages are locally developed that gradually intensified and more penetrative approaching northwestward to the Yingxiu–Beichuan Fault. This cleavage-enhancing trend implies a northwestward increase in deformation intensity. In mudstone–sandstone interlayered rocks, competence contrast facilitates the formation of layer-parallel slip and shearing. Sigmoid lens as well as "cold" shear-band fabrics consistently indicate a top-to-the-SE thrusting (Figures 3a and 6h).

In the Autochthon, lower Jurassic strata and overlying continuous Cretaceous–Cenozoic sequences are mostly concordantly folded in a long-wavelength way. The fact that early Jurassic rocks locally overturned to the southeast (North to the Tangbazi town; Figure 2) therefore implies a post-Jurassic reactivation of the SE-directed thrusting (Figures 2 and 4d).

3.3.2 Top-to-the-NW/N thrusting in the Northwestern Zone (D_{1W})

The structures and kinematics within the Northwestern Zone are different from those within the Southeastern Zone. In the northern Northwestern Zone, S-dipping foliation and associated downdip lineation are well developed. Lineations are defined by aligned calcite, fine-grained white mica, and oxide pods (Figures 2, 3a and 7a). Along the lineation, a consistent top-to-the-N/NW shearing and thrusting is determined by various kinematic indicators, such as sigma-shaped pebbles in strongly sheared meta-conglomerate (Figures 3a and 7b) and asymmetric pressure shadow in sandy–pelitic schist. Photomicrographs show that quartz ribbon (Figures 3a and 7c) and sigma-shaped feldspar porphyroclasts (Figures 3a and 7d) both indicate a top-to-the-N thrusting. In the north of the Pingwu city, greywacke and siltstone were extensively folded verging to the north with associated meter-scale reverse fault cutting fold limbs (Figures 3a and 7e). West to the Pingwu city, bedding (depicted by compositional banding) completely

transposed to SE-dipping foliations in response to the northward shearing and thrusting (Figures 3a and 7f).

In the southern Northwestern Zone, axial planar cleavage developed in the thin-bedded limestone mostly dips to the SE but strikes roughly along the margin of the Xuelongbao complex (Figure 2). On the foliation, lineation plunges to the SE at ~65–70° (Figures 2 and 3a). Along the lineation, asymmetric pressure shadow of calcite tail around garnet pseudomorph indicates a top-to-the-NW thrusting (Figures 3a and 7g). Asymmetric NW-verging folds are developed at different scales. The late Triassic turbidite was involved in a hundred-meter scale chevron fold verging to the NW that is consistent with the top-to-the-NW thrusting (Figures 3a and 7h). In the whole Northwestern Zone, the top-to-the-NW/N thrusting is indicated by the pervasive NW/N-overturned bedding as well (Figure 2)(BGMRSP, 1991).

3.3.3 Syntectonic (D_{1W}) Mupi pluton in the Northwestern Zone

In the Northwestern Zone, north of the Pingwu city, the Mupi pluton is a coarse-grained diorite and granodiorite pluton with prominent syntectonic features (Figure 2). At its southern margin, the contact between the pluton and the country rock is rather ambiguous. Strong mylonitisation with S-dipping foliation deformed both the country rocks and the south margin of the pluton (Figures 3a and 8c). On the S-dipping foliation (S_1), aligned biotite and sheared feldspar define a mylonitic lineation plunging south at ~45–75°. Kinematic indicators including sigmoidal feldspar porphyroclasts and shear-bands both indicate a top-to-the-N shearing related to thrusting (Figures 3a and 8d). About 10–15 meters northwards from the south margin of the pluton, a set of quartz + feldspar veins parallel to the shear foliation (Figures 3a and 8b), in which the quartz and feldspar did not record ductile deformation. Further north ~30 meters from the south margin of the pluton, the pluton rocks show magmatic fabric with euhedral feldspar randomly distributed (Figures 3a and 8a). Cracks in feldspar grains are sub-parallel to the shear planes and infilled with quartz (Figures 8e and S1). These cracks in conjunction with the foliation-parallel quartz + feldspar veins indicate that a brittle deformation of the feldspar occurred in the presence of residual melt. Therefore, based on the textural criteria proposed by Paterson et al. (1989), we prefer to interpret the Mupi pluton as a syntectonic one relating to the D_{1W} deformation.

3.4 Top-to-the-NW normal faulting along the northwest boundary of the basement complexes (D_2)

Most of the Neoproterozoic basement complexes in the Southeastern Zone are devoid of ductile deformation but characterized by widespread subhorizontal joints (Xue et al., 2017). Mylonite is localized along the northwest boundary of the Xuelongbao and Pengguan complexes. Along the western boundary of the Xuelongbao complex, foliation dips to the NW at 45–80° with lineation plunging to the west (Figure 2). These structural foliations and lineations are difficult to distinguish from those of the D_{1E} deformation structures. However, sigmoidal feldspar clasts and S/C fabric indicate different kinematics of top-to-the-NW normal faulting (Figures 3a and 9a). The Silurian rock directly overlies the Neoproterozoic Pengguan complex also supports NW-ward normal faulting (Figure 2).

Along the northwest boundary of the Pengguan complex, mylonitic foliation dips to the NW at high angles of ~80° (Figures 3a and 9b) with lineation steeply plunging to the NW, except for a few SE- or N-dipping foliations that probably resulted from tilting of the original foliations by the Cenozoic deformation (Figure 2). Photomicrographs including asymmetric mica fishes (Figures 3a and 9c), sigmoidal feldspar porphyroclasts (Figures 3a and 9d), and S/C fabric of white mica (Figures S2c and e) indicate a top-to-the-NW normal faulting. The deformed rocks experienced syntectonic greenschist-facies metamorphism with a mineral assemblage of quartz + feldspar + biotite + white mica + chlorite (Figures S2e–f).

Microscopic structures from the northwest Pengguan complex show sigma-shaped porphyroclast, quartz ribbon (Figures 3a and 9f), and white mica shear-band fabric (Figures 3a and 9g), indicating a top-to-the-SE shearing related to the D_{1E} deformation. However, all these structures are cut by NW-dipping shear-bands (Figures 3a and 9e). In the western flank of the Wulong complex, about 60 km southwest to the Pengguan complex, a similar top-to-the-NW normal fault with greenschist-facies metamorphism that cuts D_{1E}-related thrust sheet has been previously reported as well (Figure 1b)(Burchfiel et al., 1995; Tian et al., 2016; Airaghi et al., 2018b). Thus, we interpret the top-to-the-NW normal faulting in the northwest Pengguan complex and the Xuelongbao complex as the D_2 event after the D_{1E} top-to-the-SE thrusting in the Southeastern Zone.

4. Geochronological constraints

In order to constrain the timing of the D_1 double-vergent thrusting and the D_2 top-to-the-NW normal faulting, SIMS U–Pb dating on zircons from the synkinematic Mupi pluton and ^{40}Ar-^{39}Ar dating on metamorphic white mica, biotite and fine-grained white mica were carried out.

4.1 Analytical methods

4.1.1 Zircon SIMS U-Pb dating

Zircon concentrates were extracted using conventional crushing and separation techniques. After set in epoxy resin mounts, mineral grains were polished to their cores. Cathodoluminescence (CL) imaging was performed to observe their internal structure and find suitable positions for spot analyses. Geochronological data were acquired at the State Key Laboratory of Lithospheric Evolution, Institute of Geology and Geophysics, Chinese Academy of Sciences (IGGCAS).

U–Pb zircon dating was conducted on a Cameca IMS–1280HR SIMS following the analytical procedures described by Li et al. (2009). The primary O^{2-} ion beam was focused to elliptical spots with the sizes of 20 μm×30 μm. Measured Pb/U ratios were calibrated relative to the zircon standard Plešovice (Sláma et al., 2008). Non-radiogenic Pb was subtracted from the measured Pb isotopic composition using the measured ^{204}Pb and the present-day average terrestrial Pb isotopic composition in the model of (Stacey and Kramers, 1975). U–Pb data were plotted and calculated using the program Isoplot 3.00 (Ludwig, 2003), and age uncertainties are quoted at the 95% confidence level except for those noted otherwise. Measurements on a second zircon standard Qinghu were interspersed with unknowns to monitor the external uncertainties, and yielded concordia ages of 159.6 ± 1.6 Ma (MSWD = 0.28, N = 6), which are identical within errors to the recommended age (159.5 ± 0.2 Ma)(Li et al., 2013b).

4.1.2 ^{40}Ar-^{39}Ar dating

Micas were separated from eight micaschist, gneiss, and mylonite samples for $^{40}Ar/^{39}Ar$ dating by step-heating technique. Minerals were irradiated and measured in the Ar-Ar Laboratory, School of Earth Sciences of the University of Melbourne. Hand-picked grains were cleaned in de-ionized water and acetone. Samples were weighted and loaded into aluminum packets for irradiation. The packets were placed in a silicate glass tube (Can UM#80), interleaved with packets containing the flux monitor Mount Dromedary Biotite (Age = 99.125 ± 0.076 Ma)(Phillips et al., 2017). The canister was

irradiated for 40 MWhr in the CLICIT facility of the Oregon State University TRIGA reactor, USA. The measured isotopic ratios were corrected for system blanks, mass discrimination, and irradiation-induced interference. Plateau and/or total gas ages with 2σ uncertainties were calculated and calibrated based on methods proposed by (Lee et al., 2006). Analytical data are presented in Table S2 (Xue et al., 2020), and the age spectra are presented in Figure 11. Argon age plateaus are defined by contiguous gas fractions that together represent more than 50% of the total ^{39}Ar released from the sample and for which no difference in age can be detected between any two fractions at the 95% confidence level (Fleck et al., 1997). According to this definition, all argon age spectra in this work, except for sample CX33, do not yield plateau ages (Figure 11). We choose contiguous steps within 95% confidence close to 50% of the total ^{39}Ar released (CX6A white mica), or contiguous steps close to 95% confidence more than 50% of the total ^{39}Ar released (CX2, CX6B, CX25, CX44 white mica), to calculate weighted mean ages (Figure 11).

4.2 Results

4.2.1 U–Pb dating on synkinematic Mupi pluton

Zircons from the Mupi pluton are pink to colorless, 80 to 200 μm long with length/width ratios from 2 to 3. They show well-developed crystal morphologies. CL images of zircons show that most of the zircons have well-developed oscillatory zoning of igneous origin and some grains have an inherited core (Figure 10a). Under guidance of the zircon CL images, analyzed spots were positioned on the oscillatory zircon mantle/margin when there are exist inherited zircon cores. SIMS U–Pb zircon results are listed in Table S1. The SIMS U–Pb dating of the Mupi pluton yields a concordant age of 219.1 ± 1.7 Ma (MSWD = 0.99, N = 15; Figure 10b).

4.2.2 ^{40}Ar-^{39}Ar dating

Sample CX44 collected from the northern Northwestern Zone (Figure 12) is micaschist with penetrative SSE-dipping foliation and associated S-plunging lineation related to the D_{1W} top-to-the-N thrusting. The CX44 micaschist contains domains rich in fine-grained white mica and quartz that define the shear foliation (Figures S2a–b). Multi-grain white mica (211–152 μm) separated from CX44 yields a weighted mean age of 224.1 ± 1.7 Ma, accounting for 81% of released ^{39}Ar (Figures 11a and Table 1).

554 Sample CX12 collected from the southern Northwestern Zone (Figure 12) is
555 micaschist involved in the D_{1W} top-to-the-NW thrusting. Shear foliation is defined by
556 aligned fine-grained white mica (Figure 7g). Two aliquots of fine-grained white mica
557 (104–66 μm) of CX12A & CX12B show discordant stair-shaped spectra increasing
558 from ~65–70 Ma to ~150 Ma and ~120 Ma, respectively (Figures 11b–c and Table 1).
559 Samples CX6 and CX33 (Figure 12), collected from the Inner Metamorphic Core
560 within the Southeastern Zone, are characterized by penetrative NW-dipping foliation
561 and NW-plunging lineation that was involved in D_{1E} top-to-the-SE thrusting. In these
562 two samples, the foliations and associated lineations are defined by white mica (Figures
563 6d and S2g). Two aliquots of white mica (152–211 μm) of CX6A and CX6B yield
564 equivalent weighted mean ages of 124 ± 1.9 Ma and 126.3 ± 3.3 Ma, respectively
565 (Figure 11d–e). Multi-grain white mica (152–211 μm) from CX33 yields a plateau age
566 of 148.2 ± 1.2 Ma (>60% of the total ^{39}Ar; Figure 11f and Table 1).
567 Samples CX25 from micaschist of the Xuelongbao complex and CX18, CX19 from
568 gneiss/mylonite of the Pengguan complex (Figures 12) show well-developed NW-
569 dipping foliations related to the D_2 top-to-the-NW normal faulting (Figures S2c–f).
570 White mica (211–152 μm) in CX25 that defines the shear planes (Figures S2e–f) was
571 selected for $^{40}Ar/^{39}Ar$ dating. Five steps of sample CX25 with ~80% released ^{39}Ar
572 yields a weighted mean age of 79.7 ± 2.7 Ma (Figure 11h). Samples of CX18 and CX19
573 have stair-shaped spectra, in which ages increase from ~50–60 Ma to ~110–135 Ma
574 from low- to high-temperature steps (Figure 11i–k and Table 1).
575 Sample CX2 from the northwest boundary of the Pengguan complex (in a structural
576 position equivalent to the samples CX18 and CX19; Figure 12) was involved in the D_2
577 top-to-the-NW normal faulting (Figures 3 and 9g–i). Multi-grain white mica (211–152
578 μm) from CX2 yields a weighted mean age of 26.23 ± 0.99 Ma at low- to medium-
579 temperature steps (>50% of the total ^{39}Ar released; Figure 11g and Table 1).
580
581 4.3 Interpretation of the geochronological results
582 4.3.1 Zircon U-Pb data interpretation
583 In the northern Northwestern Zone, the Mupi pluton shows a continuous transition
584 from mylonitic fabrics along the pluton margin to magmatic fabrics in the pluton
585 interior, arguing for its synkinematic emplacement. This deduction is supported by the
586 fact that quartz + feldspar veins parallel to the mylonitic foliation, and feldspar records

brittle deformation occurred in the presence of residual melt (see details in Section 3.3.3). Thus, the D_{1W} top-to-the-N/NW thrusting is closely related to the emplacement of the Mupi pluton. Our zircon U–Pb ages reveal that the Mupi pluton emplaced at *ca.* 219 Ma, therefore place age constraint on the D_{1W} top-to-the-N/NW thrusting at *ca*. 219 Ma (Figure 12).

4.3.2 ^{40}Ar-^{39}Ar data interpretation

All samples show high radiogenic ^{39}Ar and almost all steps are clustered at the horizontal ^{39}Ar/^{40}Ar axis that does not define a real inverse isochron line (Table S2; Figure S3). Most of the step-ages calculated both by using initial ^{40}Ar/^{36}Ar of 298.56 (Lee et al., 2006) and from the so-called inverse isochron show nearly no difference (Table S2). Thus, the inverse isochron ages (though identical to their weighted mean ages or plateau ages) and the fake extraneous atmosphere argon are meaningless and will not be further discussed (Figure S3; Table S2).

Concordant white mica ^{40}Ar-^{39}Ar spectra, such as those yielded by samples of CX44 (81.6% released ^{39}Ar), CX6A (49.5% released ^{39}Ar), CX6B (52.4% released ^{39}Ar), CX33 (60.1% released ^{39}Ar), CX2 (53.6% released ^{39}Ar) and CX25 (79.7% released ^{39}Ar), are typical of samples that have remained a closed system since thermal/mylonitic resetting or crystallization (Figures 11a and d–h). Similar rocks to sample CX44 recorded greenschist facies metamorphism under temperatures of 260–310 °C (chlorite + white mica multi-equilibrium thermometer; Liu et al., 2008), which is lower than the white mica argon closure temperature of *ca.* 425 °C (100 μm grain)(Harrison et al., 2009). Considering that the dated mica grains are strongly deformed by the top-to-the-N/NW thrusting, we, therefore, interpret that the 224.1 ± 1.7 Ma argon age of CX44 recorded the timing of the white mica recrystallization related to the D_{1W} thrusting event.

Samples of CX6A & CX6B, and CX33 from the Inner Metamorphic Core, CX2 and CX25 from the mylonite zone along the northwest boundary of the Pengguan and Xuelongbao complexes have been deformed and metamorphosed at temperatures of >530°C (Raman Spectroscopy on Carbonaceous Material; Robert et al., 2010b). These temperatures are higher than the closure temperature (425 °C) of the *ca*. 100 μm radius muscovite grain (Harrison et al., 2009). There is no evidence of any post late Cretaceous to Cenozoic magmatism along the LMTB and its adjacent eastern Songpan–Ganzi Terrane. Thus, the flattened spectra of CX6A (124 ± 1.9 Ma), CX6B (126.3 ±

3.3), CX33 (148.2 ± 1.2 Ma), CX2 (26.2 ± 0.9 Ma), and CX25 (79.7 ± 2.7 Ma) are probably cooling ages when deformation rapidly exhumed those rocks through the ca. 425 °C geothermal depth. These cooling ages, therefore, can represent the timing of deformations. In this scenario, considering samples of CX6A, CX6B and CX33 were involved in top-to-the-SE thrusting, we interpret the dates of 148 Ma and 124 Ma as ages to SE-ward thrusting and rapid exhumation. Samples of CX2 and CX25 collected from the northwest boundary of the Pengguan and Xuelongbao complexes were involved in top-to-the-NW normal faulting, which may imply that the top-to-the-NW normal faulting occurred at *ca.* 27 Ma along the northwest boundary of the Pengguan complex, and at *ca.* 80 Ma along the northwest boundary of the Xuelongbao complex, respectively.

Discordant stair-shaped spectra, such as those observed from the samples of CX12, CX18, and CX19 (Figures 11b–c, i–k), are commonly observed in fine-grained mineral mixes (Tian et al., 2016). Those staircase spectra indicate ^{40}Ar diffusive loss that is possibly related to chemical alteration, a subsequent thermal event disturbance, or argon loss during the late stage mylonitisation (Costa and Maluski, 1988; Lovera et al., 1989; West and Lux, 1993). The oldest age of the stair-shaped spectra is a minimum one for the fine-grained white mica closure age (McDougall and Harrison, 1988). Samples of CX12, CX18, and CX19 have been deformed at temperatures >530°C as well (Raman Spectroscopy on Carbonaceous Material; Robert et al., 2010). Considering the size of white mica (104–66 μm), the argon-argon system of fine-grained mica should be completely reset (Harrison et al., 2009). According to the stair-shaped spectra, samples of CX12A, CX12B, CX18, CX19A, CX19B may have recrystallized or been reset before 146.5 ± 2.7 Ma, 119 ± 1.3 Ma, 111.1 ± 0.2 Ma, 133.7 ± 3.3 Ma, and 139.3 ± 1.1 Ma, respectively (Figures 11b–c, i–k). These oldest ages of the stair-shaped spectra possibly resulted from the 148–124 Ma mylonitisation as implied by ^{40}Ar-^{39}Ar cooling ages of CX6A, CX6B, and CX33.

Chemical alteration should have led to a more profound influence on the fine-grained white mica of CX12, CX18, and CX19 that may result in ^{40}Ar diffusive loss and flattened spectra (Harrison et al., 2009). In this way, considering samples of CX2, CX18, CX19, and CX25 located at the same structural position along the northwest boundary of the Neoproterozoic complexes, we may expect that CX2 and CX25, showing stair-shaped spectrum and CX18, CX19 and presenting flattened spectra, yield

younger ages, however, it is not the case (Figures 11g–k). Thus, chemical alteration and related ^{40}Ar diffusive loss may not be the main factor to account for the stair-shaped spectra.

An alternative interpretation may suggest that the youngest age of the stair-shaped spectra gives a maximum age of the thermal overprint or late-stage mylonitisation (Costa and Maluski, 1988; Lovera et al., 1989; West and Lux, 1993). As stated above, no magmatism of late Mesozoic–Cenozoic ages has been reported along the LMTB. Thus, the post-cooling thermal event may not be responsible for the minimum ages of the stair-shaped spectra. The youngest ages in the stair-shaped spectra therefore most likely indicate late-stage mylonitisation after ~60–50 Ma (Figures 11i–k), which possibly related to the *ca*. 27 Ma top-to-the-NW faulting along the northwest boundary of the Pengguan complex. It is worth to note that the CX12A and CX12B fine-grained white mica from the Northwestern Zone (Figure 12), far away from the Pengguan complex, show older minimum ages of 64.7 ± 1.3 Ma and 72.2 ± 1.4 Ma comparing with the 50 ± 0.1 Ma, 59 ± 0.3 Ma, and 58.4 ± 0.4 Ma of the CX18, CX19A and CX19B (Figures 11b–c, j–l), which may suggest that the CX12 has been less affected by the top-to-the-NW normal faulting comparing to the CX18 and CX19.

5 Discussion

5.1 Summary of our newly obtained structural results

On the basis of detailed structural analyses, a Main Central Boundary and a D_{1W} top-to-the-N/NW thrusting in the Northwestern Zone are argued for the first time in the LMTB. The Main Central Boundary corresponds to a major tectonic boundary supported both by field structures and geophysical profile (Jia et al., 2006; Robert et al., 2010b), which divides the LMTB into a Northwestern Zone (part of the Songpan–Ganzi Terrane) to the northwest and a Southeastern Zone to the southeast. The Southeastern Zone is characterized by exclusively NW-dipping foliations and associated D_{1E} top-to-the-SE thrusting, while the Northwestern Zone is characterized by exclusively SE-dipping foliations and associated D_{1W} top-to-the-NW thrusting.

This study subdivides the Southeastern Zone of the LMTB into four units based on increasing deformation intensities and metamorphic grades from southeast to northwest, namely the Autochthon, Para-autochthon, Allochthon, and Inner Metamorphic Core. This subdivision pattern is revised from the previous one that divided the LMTB into

686 an allochthonous sheet thrust southeastwards on top of the autochthonous Sichuan
687 Foreland Basin (Xu et al., 1992; Burchfiel et al., 1995; Worley and Wilson, 1996).
688 In the Southeastern Zone, a D_2 top-to-the-NW normal faulting that cuts the D_{1E} top-
689 to-the-SE thrusting is recognized along the northwest boundary of the Pengguan and
690 Xuelongbao complexes.
691
692 **5.2 Polyphase deformations along the LMTB**
693 According to the geometric and kinematic features and overprinting relationship,
694 together with ^{40}Ar-^{39}Ar and zircon U–Pb data, which allow us to draw a polyphase
695 deformation sequence of the LMTB.
696 5.2.1 Timing of the D_1 main deformation event
697 Timing of the D_{1W} top-to-the-N/NW thrusting is firstly constrained by the emplaced
698 timing of the syntectonic Mupi pluton at *ca.* 219 Ma (Figure 12). Synkinematic
699 recrystallized white mica of sample CX44 that is involved in the top-to-the-N/NW
700 thrusting yields a weighted mean age of 224.1 ± 1.7 Ma, which places a second age
701 constraint on the D_{1W} top-to-the-N/NW thrusting. This newly obtained argon age is
702 consistent with previously published white mica ^{40}Ar-^{39}Ar ages at *ca*. 237–202 Ma from
703 the northern Northwestern Zone (Figure 12)(Yan et al., 2011; Yan et al., 2018). The
704 fact that the zircon U-Pb age of the Mupi pluton is *ca.* 5 Ma younger than the
705 synkinematic white mica ^{40}Ar-^{39}Ar age may suggest the Mupi pluton emplaced during
706 the late phase of the D_{1W} event. Based on the zircon U–Pb age of syntectonic Mupi
707 pluton and synkinematic white mica ^{40}Ar-^{39}Ar age, we, therefore, suggest that the D_{1W}
708 top-to-the-N/NW thrusting event occurred at *ca*. 224–219 Ma.
709 The D_{1E} top-to-the-SE thrusting within the Southeastern Zone has been constrained
710 in the late Triassic for the following arguments: 1) Field observations and seismic
711 reflection profile revealed that late Jurassic–Cenozoic rocks unconformably overly on
712 intensively folded rocks as young as late Triassic (Figures 2 and 4a–d)(BGMRSP, 1991;
713 Jia et al., 2006); 2) Detailed petrological analyses and in-situ allanite U–Pb dating and
714 biotite $^{40}Ar/^{39}Ar$ dating revealed a *ca.* 204–190 Ma peak metamorphism in the Inner
715 Metamorphic Core that postdates the D_{1E} event (Airaghi et al., 2017a; 2018a; 2018c);
716 3) The ages of the voluminous magmatism intruding the extensively folded Songpan–
717 Ganzi Terrane range between 223 and 200 Ma, which postdates the folding in the
718 Songpan–Ganzi Terrane and the top-to-the-SE thrusting of the LMTB (Figure 12)(Xu

et al., 1992; Roger et al., 2004; Harrowfield and Wilson, 2005; Hu et al., 2005; Zhang et al., 2007; de Sigoyer et al., 2014). Thus, the regional D_{1E} top-to-the-SE thrusting was at least activated during the late Triassic, together with the contemporary D_{1W} top-to-the-N/NW thrusting recorded within the Northwestern Zone, both of which compose the *ca*. 224–219 Ma main D_1 double-vergent event.

5.2.2 Timing of the D_2 top-to-the-NW normal faulting

According to the newly obtained ^{40}Ar-^{39}Ar ages, the timing of the D_2 top-to-the-NW normal faulting occurred along the northwest boundary of the Pengguan (*ca.* 27 Ma) and Xuelongbao (*ca.* 80 Ma) complexes are quite different. The top-to-the-NW/N normal faulting is widespread in an over 300 km long zone along the northern margins of the Danba and Kangding complexes, and the northwest margins of the Baoxing, Wulong, Xuelongbao, Moutuo, Pengguan, and Jiaoziding complexes (Figure 12)(Burchfiel et al., 1995; Xu et al., 2008; Tian et al., 2016; Xue et al., 2017). This belt of top-to-the-NW normal faulting has previously been entitled East Tibet Detachment (Figure 12)(Wang et al., 2012b). Timing of the East Tibet Detachment top-to-the-NW normal faulting is different at different localities. Hames and Burchfiel (1993) reported a top-to-the-NW normal faulting and syntectonic metamorphism at *ca.* 25 Ma along the northwest Pengguan complex that is in accordance with the *ca*. 27 Ma top-to-the-NW normal faulting as indicated by sample CX2 (Figure 12).

Along the northwest boundary of the Wulong complex and north boundary of the Danba complex, the top-to-the-NW/N normal faulting was constrained to *ca.* 81–47 Ma ($^{40}Ar/^{39}Ar$ dating on metamorphic biotite and white mica; Figure 12)(Zhou et al., 2008; Tian et al., 2016). This phase of the top-to-the-NW normal faulting is recorded along the northwest boundary of the Xuelongbao complex (*ca.* 80 Ma ^{40}Ar-^{39}Ar age of sample CX25) as well.

A period of the top-to-the-NW/N normal faulting at *ca.* 166–159 Ma was reported at the northwest boundary of the Jiaoziding and Pengguan complexes, and the north boundary of the Danba complex (Figure 12)(Dirks et al., 1994; Zhou et al., 2008; Li, 2009). Whereas, younger ages of *ca*. 122–120 Ma related to the top-to-the-N normal faulting at the north boundary of the Danba complex were reported as well (Figure 12)(Xu et al., 2008).

In summary, the timing of the top-to-the-NW normal faulting of the East Tibet Detachment are scattered at *ca.* 166–159 Ma (north Danba, northwest Pengguan,

752 northwest Jiaoziding), *ca.* 122–120 Ma (north Danba), *ca.*81–47 Ma (north Danba,
753 northwest Wulong) and *ca.* 27–25 Ma (northwest Pengguan; Figure 12). Nonetheless,
754 a process is required to explain these four groups of well-defined argon plateau ages
755 that do not show an age-changing trend in map view (Figure 12). We, therefore, prefer
756 to interpret that the top-to-the-NW/N normal faulting of the East Tibet Detachment was
757 episodically and co-planarly activated at *ca.* 166–159 Ma, *ca.* 122–120 Ma, *ca.* 81–47
758 Ma, and *ca.* 27–25 Ma (Figure 12). The late-stage activations could partially reset the
759 fine-grained white mica argon system that resulted in stair-shaped spectra yielded by
760 samples of CX18 and CX19 (Figures 11 and 12).
761
762 **5.3 Episodic basement-slice-imbrication and amphibolite facies metamorphic rock**
763 **exhumation**
764 The Western Sichuan Foreland Basin (WSFB) was formed by loading and
765 subsidence due to the southeastward thrusting of the LMTB along the Yingxiu–
766 Beichuan Fault and Xiaoguanzi Fault (T_2 in Figure 12)(Chen and Wilson, 1996; Li et
767 al., 2003). Episodic terrestrial deposition in the WSFB from the late Triassic to the
768 present day indicates that the LMTB continued to be tectonically active episodically
769 during the late Triassic to early Jurassic, late Jurassic to early Cretaceous, and late
770 Cretaceous to earliest Paleocene (Figure 12)(Xu et al., 2008; Li et al., 2013c; Tian et
771 al., 2016).
772 The late Jurassic to early Cretaceous southeastward thrusting of the Yingxiu–
773 Beichuan Fault and Xiaoguanzi Fault (T_2 in Figure 12), as the southeast boundary Fault
774 of the Pengguan and Baoxing complexes, overlaps the *ca.* 166–159 Ma and *ca.* 122–
775 120 Ma top-to-the-NW/N normal faulting along the NW boundary of the Jiaoziding
776 complex and the north boundary of the Danba complex (Figure 12)(Xu et al., 2008;
777 Zhou et al., 2008; Li, 2009). The late Cretaceous–earliest Paleocene southeastward
778 thrusting of the Yingxiu–Beichuan Fault and Xiaoguanzi Fault is also coeval with the
779 top-to-the-NW/N normal faulting along the NW boundary of the Xuelongbao (CX25
780 in this study) and Wulong (Tian et al., 2016) complexes (Figure 12). Furthermore, both
781 the top-to-the-SE thrusting and top-to-the-NW normal faulting along the southeast and
782 northwest boundaries of the complexes occurred under similar greenschist-facies
783 metamorphic conditions (Airaghi et al., 2017b; Xue et al., 2017). Conjugated
784 kinematics of boundary SE-thrusting and NW-normal faulting characterized by similar

metamorphic conditions and synchronous timing let us propose that the Xuelongbao, Pengguan, Baoxing and Wulong complexes were episodically imbricated to the southeast as basement-slices during late Jurassic–early Cretaceous and late Cretaceous–earliest Paleocene.

Numerical modeling of co-seismic slip vectors *vs*. fault angles indicates that the latest high-angle listric Yingxiu–Beichuan Fault might have facilitated the vertical imbrication of the Pengguan complex with no need of the SE-ward thrusting and loading (Feng et al., 2015). This feature explains the absence of a rejuvenated foreland basin contemporary to the 27–25 Ma basement imbrication. Nevertheless, the 27–25 Ma basement slice imbrication of the Pengguan complex is compatible with its 30–25 Ma fast cooling (Figure 12)(Wang et al., 2012a).

In the map view, two amphibolite facies metamorphic zones wrap the Xuelongbao and Danba complexes (Figure 13a). Both amphibolite facies metamorphic zones reached peak conditions at *ca*. 210–180 Ma post to the late Triassic orogeny (Figure 12)(Dirks et al., 1994; Huang et al., 2003a; Weller et al., 2013; Airaghi et al., 2018a). Gravity anomaly indicated that the Xuelongbao complex probably extends northeastwards beneath and parallel to the amphibolite facies metamorphic rocks (Xue et al., 2017). Coincidently, the Wenchuan–Xuelongbao and Danba amphibolite facies metamorphic zones experienced rapid exhumation and cooling during the late Jurassic to early Cretaceous (CX12 and CX33 in this work) that is coeval with the aforementioned late Jurassic–early Cretaceous basement-slice-imbrication (Figure 13b)(Arne et al., 1997; Huang et al., 2003a; Tian et al., 2016; Airaghi et al., 2018a). Both gravity inversion (Xue et al., 2017) and seismic reflection profiles (Guo et al., 2013) revealed a belt of basement-slice hidden right beneath a Mesozoic Laojungou granite (224 ± 5 Ma; Zhao et al., 2007) within the east Songpan–Ganzi Terrane (Figure 13a). The Laojungou granite recorded rapid exhumation and cooling during the late Jurassic to early Cretaceous as well (Figure 13b)(Yuan et al., 1991).

Considering the spatial–cooling–imbricating relationships between the Laojungou granite, amphibolite facies metamorphic zones and basement-slices, we interpret that the Laojungou granite and amphibolite facies metamorphic rocks were popped up by a basement-slice-imbrication during the late Jurassic–early Cretaceous. The basement-slice-imbrication was responsible for localized fast cooling and exhumation of the amphibolite-facies metamorphic rocks. However, the Wenchuan–Xuelongbao

metamorphic sedimentary cover does not show fast cooling during the late Cretaceous–earliest Paleocene and at *ca.* 27–25 Ma comparing to the basement-slice-imbrication (Figure 13b), which needs further work.

5.4 Mesozoic tectonic evolution of the LMTB

The Mesozoic tectonic evolution of the LMTB can be summarized as follows without consideration of the top-to-the-N/NW thrusting in the Northwestern Zone. Namely, the Songpan–Ganzi Terrane subducted to the north along the Anymaqen Suture Zone and/or to the southwest along the Jinshajiang Suture Zone, which resulted in the top-to-the-S shearing of the thick Triassic flysch cover along a basal decollement layer (Mattauer et al., 1992; Calassou, 1994) and associated sinistral strike-slip to the southeastward thrusting in the LMTB (Xu et al., 1992; Dirks et al., 1994; Burchfiel et al., 1995; Worley and Wilson, 1996; Roger et al., 2004; Harrowfield and Wilson, 2005). The amphibolite facies metamorphism in the Wenchuan–Xuelongbao area reached the peak pressure of > 11 ± 2 kbar at *ca*. 200 Ma (Airaghi et al., 2018b) required a sedimentary cover more than 30 km in thickness. However, high-resolution seismic reflection and gravity modeling profiles revealed a ~20 km thickness cover of the Songpan–Ganzi Terrane (Guo et al., 2013; Xue et al., 2017) that is far thinner than the required ~30 km thickness.

In contrast, Sengör (1984) and Luo (1991) regarded the LMTB as an early Mesozoic intracontinental subduction zone but lack details of structural observation. Considering the pervasive top-to-the-N/NW thrusting in the Northwestern Zone and top-to-the-SE thrusting in the Southeastern Zone, we thus prefer an early Mesozoic intracontinental subduction along the LMTB.

In this work, the Main Central Boundary, devoid of ophiolitic rocks separating the Southeastern Zone to the SE from the Northwestern Zone to the NW, does not represent an ophiolitic suture zone, but a tectonic “scar” corresponding to the place where the Yangtze basement was underthrusted. Like the Chenzhou–Linwu Fault in the Xuefengshan Intracontinental Orogen (South China) where the South China Block underthrusted (Chu et al., 2012a; Chu et al., 2012b). Along the LMTB, the underthrusting was coeval with important burial (> 11 ± 2 kbar) and the double-vergent thrusting in both sides of the Main Central Boundary. The basement underthrusting is also supported by the blueschist with intraplate affinity reported along the Qingchuan–

Pingwu Fault (Wei, 1994; Xu et al., 2020). A new tectonic scenario is proposed here (Figure 14). In the pre-middle Triassic times, the Longmenshan area along the western Yangtze margin was a failed rift evidenced by radiolarian chert, abyssal deposits, slump structures (Long, 1991; Luo, 1991; Chang, 2000; Li, 2009) and seismic profile (Jia et al., 2006). Accompany with the pre-middle Triassic rifting, a series of NW-dipping syn-depositional normal faults developed in the Longmenshan area that dissected the western Yangtze basement to slices, and the lower crust thinned significantly that resulted in a local "weak zone" in the lower crust (Figure 14a).

During the late Triassic, the Yangtze basement underthrusting along the "weak zone" accommodated by inversion of the normal faults, which can be linked to the far-field effect of the Paleotethys' closure (Figure 14b)(Luo, 1991; Chen and Wilson, 1996; Meng et al., 2005; Yan et al., 2019). The sedimentary cover was simultaneously shortened by a top-to-the-SE thrusting and a top-to-the-NW thrusting associated with the main D_1 event (Figure 14b). The domain of the top-to-the-SE thrusting in the Southeastern Zone is larger and more extensive than the top-to-the-NW thrusting in the Northwestern Zone. Similar structures were developed in the north Himalaya where a large domain experienced a top-to-the-S thrusting, compared to a small domain with a top-to-the-N thrusting due to the northward subduction of the India plate (Dewey, 1988; Harrison, 1992). We thus favor an NW-ward basement underthrusting along the LMTB (Figure 14b). The large amount of rift rocks transported southeastwards and overlain the autochthonous foreland basin. In addition, a large volume of rocks was underthrusted to crustal depth deeper than 30 km and metamorphosed, as documented by the *ca*. 210–180 Ma amphibolite-facies metamorphic zone that metamorphosed at a peak pressure of > 11±2 kbar (Figure 12)(Weller et al., 2013; Airaghi et al., 2018a; Airaghi et al., 2018b; Airaghi et al., 2018c).

During periods of the late Jurassic–early Cretaceous, late Cretaceous–earliest Paleogene, the accretion of Gondwana-derived Terranes to the southern Eurasia plate had resulted in episodic compression in the Longmenshan area (Dewey, 1988; Xu et al., 1992). We cannot rule out the possible contribution of the 150–140 Ma and 120–105 Ma compression resulted from the westward subduction of the Paleo-Pacific plate subduction (Chu et al., 2019). Under the regional episodic compression, basement-slices represented by the Neoproterozoic complexes along the weak zone of the Yangtze Block, including the Xuelongbao, Moutuo, and Danba complexes,

episodically imbricated southeastwards along the inherited faults. Basement-slice-imbrication then exhumed the basement complexes and the amphibolite facies metamorphic rocks as documented by the synchronously fast cooling of the meta-sediments and the basement complexes (Figures 12 and 14d)(Yuan et al., 1991; Arne et al., 1997; Huang et al., 2003b; Weller et al., 2013; Tian et al., 2016). Basement-slice-imbrication also reworked the late Triassic allochthonous–autochthonous LMTB into four subdivisions (Figure 14d).

7 Conclusions

Based on structural analysis and previous geophysical profile, we have delineated a Main Central Boundary that separates the Longmenshan Thrust Belt into a Southeastern Zone to the southeast and a Northwestern Zone to the northwest.

On the basis of different lithologies, increasing strain intensity and metamorphic grade, the Southeastern Zone is revised into four subdivisions, namely, the Autochthon, Para-autochthon, Allochthon, and Inner Metamorphic Core.

The detailed structural analysis allows us recognizing the multiphase deformation of the LMTB. A main D_1 double-vergent thrusting event, characterized by the D_{1E} top-to-the-SE thrusting in the Southeastern Zone and the D_{1W} top-to-the-NW/N thrusting in the Northwestern Zone, has been recognized. The D_{1E} and D_{1W} events were synchronously occurred corresponding to a late Triassic intracontinental underthrusting along a "weak zone" of the LMTB. A D_2 top-to-the-NW normal faulting that cuts the D_{1E} top-to-the-SE thrusting has been recognized along the NW boundary of the basement complexes in the Southeastern Zone.

Geochronological constraints obtained from this study and the previously published ones indicate that the main D_1 event occurred at *ca*. 224–219 Ma and the D_2 was episodically activated at *ca.* 166–160 Ma, 141–120 Ma, 81–47 Ma, and 27–25 Ma. The episodically and synchronously activated top-to-the-NW normal faulting and top-to-the-SE thrusting along the northwest and SE boundaries of the basement complexes let us propose that the basement-slices episodically imbricated to the SE during the late Jurassic–early Cretaceous and late Cretaceous–earliest Paleocene. The basement-slice imbrication exhumed the D_1-related amphibolite facies rocks to the subaerial and reworked allochthonous–autochthonous LMTB into a four subdivision one.

Acknowledgement

This work is supported by the National Nature Science Foundation of China (91855212, 91755205 and 41802219) and the National Key R&D Program of China (Grant Numbers 2016YFC0600401, 2016YFC0600102) as well as French LABEX VOLTAIRE (ANR-10-LABX-100-01), and EQUIPEX PLANET (ANR-11-EQPX-0036). Two anonymous reviewers are sincerely thanked for their elaborative reviews and pertinent comments. The geochronological data including SIMS U–Pb dating on zircons (Table S1) and $^{40}Ar/^{39}Ar$ dating on micas (Table S2) for this paper are available in the supplementary materials.

Figure captions

Figure 1. (a) Simplified tectonic sketch of China. QLDB: Qingling–Dabie Orogenic Belt; EKL–ANMQS: East Kunlun–Anymaqen Suture Zone; JSZ: Jinshajiang Suture Zone; SGT: Songpan–Ganzi Terrane; LMTB: Longmenshan Thrust Belt; ICB: Indochina Block; (b) Simplified geological map of the Longmenshan Thrust Belt, modified after BGMRSP (1991), Burchfiel et al. (1995) and Xu et al. (2008). T_1: Anxian–Guanxian Fault; T_2: Yingxiu–Beichuan Fault; T_3: Wenchuan–Maoxian Fault; T_4: Qingchuan–Pingwu Fault; JZD: Jiaoziding complex; PG: Pengguan complex; XLB: Xuelongbao complex; BX: Baoxing complex; KD: Kangding complex; DB: Danba complex; MT: Moutuo complex; WL: Wulong complex; RLG: Rilonguan granite; LJG: Laojungou granite.

Figure 2. Geological map of the north and middle parts of the LMTB and its adjacent area, modified after BGMRSP (1991) and Xu et al. (2008). MP: Mupi pluton. Symbols and acronyms are the same as in Figure 1.

Figure 3. (a) Structural division, field elements including foliation, lineation, and kinematics of the LMTB. (b-d) π-circle projection of the bedding (S_0) in the Para-autochthon from south to north. All field elements are shown in a lower hemisphere equal-area projection. Symbols and acronyms are the same as in Figure 1.

Figure 4. (a–d) Geological cross-sections perpendicular to the LMTB. Purple solid lines represent the foliations attitude (Locations are marked in Figure 2). Subaerial structures of these cross-sections are based on our field mapping and the deep structures are based on seismic reflection data of Jia et al. (2006) and Guo et al. (2013). The black dashed lines represent speculated folds. (e) Flower structure revealed

by the seismic reflection profile processed by Jia et al. (2006)(Location is marked in Figure 4d). MCB: Main Central Boundary; AGF: Anxian–Guanxian Fault; YBF: Yingxiu–Beichuan Fault; WMF: Wenchuan–Maoxian Fault; QCF: Qingchuan–Pingwu Fault. Other symbols and acronyms are the same as in Figure 1

Figure 5. Rock characteristics and deformation style of the Main Central Boundary. (a) Intensely deformed argillaceous limestone characterized by a vertical foliation [31°34.833' N, 103°24.041' E]. (b) Graphite-bearing pelite was intensely foliated to shale with vertical attitude [31°35.916' N, 103°24.008' E]. (c) Foliated thin-bedded limestone and quartz ribbon interlayer and rootless intra-folial folds coexist with vertical foliation [31°48.403' N, 103°44.080' E]. Rootless folds in figures b–c implying significant shortening. Locations are presented in Figure 3a.

Figure 6. Structural features related to the Main Deformation (D_{1E}) in the Southeastern Zone. **In the Inner Metamorphic Core**: (a) Lineation formed by aligned biotite plunging N335° by 30° on the S-dipping foliation [31°30.359' N, 103°34.123' E]. (b) Asymmetric pyrite pressure shadow indicating a top-to-the-SE thrusting [31°42.210' N, 103°51.067' E]. (c) Sigma-shaped feldspar porphyroclast in paragneiss indicating a top-to-the-SE thrusting [31°05.193' N, 103°18.730' E]. (d) S/C fabric observed under Cross Polarized Light (CPL) indicating a top-to-the-SE thrusting. **In the Allochthon**: (e) Sigmoid pelitic lens and "cold" S/C structures developed in the Neoproterozoic Huangshuihe Group suggesting a to the top-to-the-SE thrusting [31°16.195' N, 103°46.747' E]. (f) Sigma-shaped sandy lens in Silurian pelitic schist within the nappe indicating a top-to-the-SE thrusting [32°04.577' N, 104°40.599' E]. (g) At the rear of the klippe, thick-bedded limestone thrust to the SE along an NW-dipping reverse fault [31°11.530' N, 103°45.929' E]. **In the Para-autochthon**: (h) Sigmoid lens and "cold" S/C fabrics indicating a top-to-the-SE thrusting [30°55.403' N, 103°20.495' E]. Figure locations are marked in Figure 3a. X and Z axes are marked on the figures. Mineral abbreviations are after Kretz (1983).

Figure 7. Structural features related to the Main Deformation (D_{1W}) in the Northwestern Zone. **In the northern Northwestern Zone**: (a) Aligned calcite, fine-grained white mica, and oxide-pods define lineation plunging to the south on the S-dipping foliation [32°30.892' N, 104°08.178' E]. (b) Sigma-shaped pebbles in a meta-conglomerate indicating a top-to-the-N sense of shear [32°53.562' N, 105°04.820' E]. (c) Deflected quartz ribbon observed under CPL indicating a top-to-the-N thrusting. (d) Asymmetric feldspar porphyroclast wrapped by deflected white mica suggesting a top-to-the-N thrusting. (e) Northward verging chevron fold associated with meter-scale reverse fault indicating a top-to-the-N

983 thrusting [32°25.219' N, 104°31.513' E]. (f) Bedding depicted by compositional banding showing an N-
984 verging fold, and bedding to sub-parallel to the foliation in the limbs [32°228.591' N, 104°26.763' E]. **In**
985 **the southern Northwestern Zone**: (g) Asymmetric garnet pseudomorph pressure shadow suggesting a
986 top-to-the-NW thrusting. (h) Hundred-meter scale chevron fold verging to the NW indicating a top-to-
987 the-NW thrusting [31°33.912' N, 103°16.680' E]. Figure locations are marked in Figure 3a. X and Z axes
988 are marked on the figures. Mineral abbreviations are after Kretz (1983).
989
990 Figure 8. Features of the syn-tectonic Mupi pluton in the Northwestern Zone [32°31.445' N, 104°32.456'
991 E]. (a) Magmatic fabric of the Mupi pluton with euhedral feldspar randomly distributed, about 30 meters
992 north to the south margin of the Mupi pluton. (b) Quartz + feldspar veins parallel to the shear foliation,
993 about 10-15 meters north to the pluton south margin. (c) Strong mylonitisation at the south margin of the
994 pluton shares similar structural geometry and kinematics with the country rock. (d) Asymmetric feldspar
995 porphyroclasts, synthetic offset of feldspar fragments along shear band in XZ plane indicating a top-to-
996 the-N thrusting. (e) Panorama of thin section under CPL of the Mupi pluton, the feldspar brittle cracks
997 (marked by red arrow) infilled by quartz subparallel to the shear foliation. X and Z axes are marked on
998 the figures. Figure locations are marked in Figure 3a. Mineral abbreviations are after Kretz (1983).
999
1000 Figure 9. Structural features related to the top-to-the-NW normal faulting along the northwest boundary
1001 of the Neoproterozoic complexes. (a) At the northwest boundary of the **Xuelongbao complex**, sigmoid
1002 feldspar phenocrysts associated with S/C fabric indicating a top-to-the-NW normal faulting [31°19.683'
1003 N, 103°23.874' E]. At the northwest boundary of the **Pengguan complex**: (b) Granitic mylonite having
1004 foliation dips to the NW [31°22.931' N, 103°30.364' E]. (c–d) Mica fish in the quartz schist (PPL) and
1005 σ-type porphyroclast (CPL) wrapped by deflected micas indicating a top-to-the-NW normal faulting. (e)
1006 Shear-band (white dashed line) distributes from the upper-right corner to the lower-left corner that cuts
1007 the whole thin section indicate a top-to-the-NW normal faulting, CPL. Sigmoid porphyroclast (e),
1008 incipient shear band inclining to the SE (f), and white mica shear-band fabric (g) indicate a top-to-the-
1009 SE thrusting related to D_{1E}. All of them are cut by the white shear band related to the D_2 top-to-the-NW
1010 normal faulting, CPL. Locations are marked in Figure 3a. X and Z axes are marked on the figures.
1011 Mineral abbreviations are after Kretz (1983).
1012
1013 Figure 10. (a) CL images of the representative zircons from the Mupi pluton. The scale bar represents
1014 100 μm. (b) SIMS U–Pb Concordia diagram of zircons of the syntectonic Mupi pluton.
1015

Figure 11. ^{40}Ar-^{39}Ar age spectra of the dated samples. We carried out a two-aliquot analysis of micas from CX6, CX12, and CX19 to exclude the influence of occasional deviation on the stair-case age spectrum, and the two-aliquot results are labeled with the suffix of A and B (*eg.,* CX6A, CX6B, CX12A, CX12B, CX19A, CX19B). Inverse isochron diagrams are presented in Figure S3. ^{40}Ar-^{39}calculation results are
summarized in Table 1, and detailed step-heating results are presented in the supporting information Table S2.

Figure 12. Geochronological constraints compiled from published and this study. Ages are shown by the method used to determine the age (A = Ar/Ar; K = K/Ar; U = U/Pb; F = Fission track) and mineral used (Am = Amphibole; B = biotite; M = Muscovite; Z = zircon; Mn = monazite; I= illite; S = Sericite; Wm = white mica). 1. Li (2009); 2. Yan et al. (2018); 3. Yan et al. (2011); 4. Arne et al. (1997); 5. Airaghi et al. (2017b); 6. Airaghi et al. (2018a); 7. Airaghi et al. (2018b); 8. Airaghi et al. (2018c); 9. Zheng et al. (2016); 10. Yan et al. (2008); 11. Zheng et al. (2014); 12. Tian et al. (2016); 13. Huang et al. (2003a); 14. Weller et al. (2013); 15. Xu et al. (2008); 16. Zhou et al. (2008); 17. Wallis et al. (2003); 18. Zhou et al. (2002); 19. Xia (1993); 20. Xu et al. (1992); 21. Yuan et al. (1991); 22. Hu et al. (2005); 23. Zhao (2007); 24. Kirby et al. (2002); 25. Roger et al. (2004); 26. Zhang et al. (2006a); 27. Yuan et al. (2010); 28. BGMRSP (1991); 29. Li et al. (2013c); 30. Wang et al. (2012a). 31. Hames and Burchfiel (1993). Symbols and acronyms are the same as in Figure 2.

Figure 13. (a) Spatial relationship between the amphibolite facies metamorphic zones and the basement complexes along the peripheries of the Songpan–Ganzi Terrane. Isograd lines are presented in color dashed lines accompany relating mineral abbreviations. Mineral abbreviations are after Kretz (1983) except Liq representing the magmatic zone. Symbols and acronyms are the same as in Figure 12. (b) Compiled cooling histories for the Wenchuan–Xuelongbao amphibolite facies metamorphic belt (WXAB, bold dashed line)(Airaghi et al., 2018a), the Danba amphibolite facies metamorphic belt (DBAB), and migmatite zone (DBM, thin dashed line)(Huang et al., 2003a), and the Mesozoic Laojungou granite (LJG, bold gray line)(Yuan et al., 1991). Gray frames show the three episodes of basement-slice-imbrication at late Jurassic–early Cretaceous, late Cretaceous–Earliest Paleocene, *ca*. 27–25 Ma. The Wenchuan–Xuelongbao and the Danba amphibolite facies metamorphic belt and the Laojungou granite experienced a rapid exhumation and cooling during the late Jurassic to the late Cretaceous, and 27-25 Ma.

Figure 14. A possible Mesozoic tectonic evolutionary scenario of the LMTB and adjacent area. (a) Pre-middle Triassic rifting of the Yangtze Block resulted in crustal thinning and a potential "weak zone" in the future Longmenshan area. (b) During the late Triassic, NW-ward Yangtze basement underthrusting along the "weak zone" resulted in extensive shortening, inversion of syn-depositional normal Fault. The sedimentary rocks were buried to a crustal depth deeper than 30 km. NW- and SE-ward thrusting, and associated nappe belt formed at this time. (c) During the late Triassic to early Jurassic, the underthrusted rocks were metamorphosed. Gradient color from green to dark blue in the Inner Metamorphic Core represents show the low- to high-metamorphic grade. (d) late Jurassic–Miocene, basement-slice episodically imbricated to the SE that exhumed the amphibolite facies metamorphic rocks to the subaerial and reworked the LMTB. Symbols and acronyms are the same as in Figure 2.

Table 1. Summary of ^{40}Ar-^{39}Ar dating results

References

Airaghi, L., Janots, E., Lanari, P., de Sigoyer, J., and Magnin, V., 2018a, Allanite petrochronology in fresh and retrogressed garnet-biotite metapelites from the Longmen Shan (eastern Tibet): Journal of Petrology, p. egy109-egy109, https://doi.org/10.1093/petrology/egy109.

Airaghi, L., Lanari, P., de Sigoyer, J., and Guillot, S., 2017a, Microstructural vs compositional preservation and pseudomorphic replacement of muscovite in deformed metapelites from the Longmen Shan (Sichuan, China): Lithos, v. 282-283, p. 262-280, https://doi.org/10.1016/j.lithos.2017.03.013.

Airaghi, L., Sigoyer, J., Guillot, S., Robert, A., Warren, C. J., and Deldicque, D., 2018b, The Mesozoic along-strike tectono-metamorphic segmentation of Longmen Shan (eastern Tibetan plateau): Tectonics, v. 37, p. 4655-4678, https://doi.org/10.1029/2018TC005005.

Airaghi, L., Sigoyer, J. d., Lanari, P., Guillot, S., Vidal, O., Monié, P., Sautter, B., and Tan, X., 2017b, Total exhumation across the Beichuan fault in the Longmen Shan (eastern Tibetan plateau, China): constraints from petrology and thermobarometry: Journal of Asian Earth Sciences, https://doi.org/10.1016/j.jseaes.2017.04.003.

Airaghi, L., Warren, C. J., de Sigoyer, J., Lanari, P., and Magnin, V., 2018c, Influence of dissolution/reprecipitation reactions on metamorphic greenschist to

amphibolite facies mica 40Ar/39Ar ages in the Longmen Shan (eastern Tibet): Journal of Metamorphic Geology, v. 36, no. 7, p. 933-958, https://doi.org/10.1111/jmg.12420.

Arne, D., Worley, B., Wilson, C., Chen, S. F., Foster, D., Luo, Z. L., Liu, S. G., and Dirks, P., 1997, Differential exhumation in response to episodic thrusting along the eastern margin of the Tibetan Plateau: tectonophysics, v. 280, no. 3, p. 239-256, https://doi.org/10.1016/S0040-1951(97)00040-1.

BGMRSP, 1991, Regional geology of Sichuan Province, Beijing, Geological Publishing House, 730 p.:

Billerot, A., Duchene, S., Vanderhaeghe, O., and de Sigoyer, J., 2017, Gneiss domes of the Danba Metamorphic Complex, Songpan Ganze, eastern Tibet: Journal of Asian Earth Sciences, v. 140, p. 48-74, https://doi.org/10.1016/j.jseaes.2017.03.006.

Burchfiel, B. C., Chen, Z., Liu, Y., and Royden, L. H., 1995, Tectonics of the Longmen Shan and Adjacent Regions, Central China: International Geology Review, v. 37, no. 8, p. 661-735, https://doi.org/10.1080/00206819509465424.

Burchfiel, B. C., Royden, L. H., van der Hilst, R. D., Hager, B. H., Chen, Z., King, R. W., Li, C., Lü, J., Yao, H., and Kirby, E., 2008, A geological and geophysical context for the Wenchuan earthquake of 12 May 2008, Sichuan, People's Republic of China: GSA Today, v. 18, no. 7, p. 4-11, https://doi.org/10.1130/gsatg18a.1.

Calassou, S., 1994, Etude tectonique d'une chaîne de décollement. A- Tectonique triasique et tertiaire de la chaîne de Songpan Garzê(Est Tibet). B- Géométrie et cinématique des déformations dans les prismes d'accrétion sédimentaire: Modélisation analogique.

Chang, E. Z., 2000, Geology and Tectonics of the Songpan-Ganzi Fold Belt, Southwestern China: International Geology Review, v. 42, no. 9, p. 813-831, https://doi.org/10.1080/00206810009465113.

Chen, S., and Wilson, C. J. K., 1996, Emplacement of the Longmen Shan Thrust-Nappe Belt along the eastern margin of the Tibetan Plateau: Journal of Structural Geology, v. 18, no. 4, p. 413-429. (In Chinese with english abstract)

Chen, S., Wilson, C. J. L., Luo, Z., and Deng, Q., 1994, The evolution of the Western Sichuan Foreland Basin, southwestern China: Journal of Asian Earth Sciences,

v. 10, no. 94, p. 159–168, https://doi.org/10.1016/0743-9547(94)90016-7.

Chen, S., Wilson, C. J. L., and Worley, B. A., 1995, Tectonic transition from the Songpan-Garzê Fold Belt to the Sichuan Basin, south-western China: Basin Research, v. 7, no. 3, p. 235-253, https://doi.org/10.1111/j.1365-2117.1995.tb00108.x.

Chu, Y., Faure, M., Lin, W., and Wang, Q., 2012a, Early Mesozoic tectonics of the South China block: Insights from the Xuefengshan intracontinental orogen: Journal of Asian Earth Sciences, v. 61, p. 199-220, https://doi.org/10.1016/j.jseaes.2012.09.029.

Chu, Y., Faure, M., Lin, W., Wang, Q., and Ji, W., 2012b, Tectonics of the Middle Triassic intracontinental Xuefengshan Belt, South China: new insights from structural and chronological constraints on the basal décollement zone: International Journal of Earth Sciences, v. 101, no. 8, p. 2125-2150, https://doi.org/10.1007/s00531-012-0780-5.

Chu, Y., Lin, W., Faure, M., Xue, Z., Ji, W., and Feng, Z., 2019, Cretaceous Episodic Extension in the South China Block, East Asia: Evidence From the Yuechengling Massif of Central South China: Tectonics, v. 38, no. 10, p. 3675-3702, https://doi.org/10.1029/2019tc005516.

Clark, M. K., and Royden, L. H., 2000, Topographic ooze: Building the eastern margin of Tibet by lower crustal flow: Geology, v. 28, no. 8, p. 703-706, https://doi.org/10.1130/0091-7613.

Costa, and Maluski, 1988, Use of the 40Ar-39Ar stepwise heating method for dating mylonite zones: An example from the St. Barth616my Massif (North Pyrenees, France). Chemical Geology, v. 72, no. 2, p. 127-144, https://doi.org/10.1016/0168-9622(88)90061-9.

de Sigoyer, J., Vanderhaeghe, O., Duchêne, S., and Billerot, A., 2014, Generation and emplacement of Triassic granitoids within the Songpan Ganze accretionary-orogenic wedge in a context of slab retreat accommodated by tear faulting, Eastern Tibetan plateau, China: Journal of Asian Earth Sciences, v. 88, p. 192-216, https://doi.org/10.1016/j.jseaes.2014.01.010.

Dewey, J. F., 1988, The Tectonic Evolution of the Tibetan Plateau: Philosophical Transactions of the Royal Society of London A Mathematical Physical & Engineering Sciences, v. 327, no. 1594, p. 379-413,

https://doi.org/10.1098/rsta.1988.0135.

Dirks, P., Wilson, C., Chen, S., Luo, Z., and Liu, S., 1994, Tectonic evolution of the NE margin of the Tibetan Plateau; evidence from the central Longmen Mountains, Sichuan Province, China: Journal of Southeast Asian Earth Sciences, v. 9, no. 1, p. 181-192, https://doi.org/10.1016/0743-9547(94)90074-4.

Druschke, P. A., and Wang, T., 2006, Stratigraphic and UPb SHRIMP Detrital Zircon Evidence for a Neoproterozoic Continental Arc, Central China: Rodinia Implications: Journal of Geology, v. 114, no. 5, p. 627-636.

Enkelmann, E., Weislogel, A., Ratschbacher, L., Eide, E., Renno, A., and Wooden, J., 2007, How was the Triassic Songpan-Ganzi basin filled? A provenance study: Tectonics, v. 26, no. 4, https://doi.org/10.1029/2006TC002078.

Feng, S., Zhang, P., Liu, B., Wang, M., Zhu, S., Ran, Y., Wang, W., Zhang, Z., Zheng, W., and Zheng, D., 2015, Deep crustal deformation of the Longmen Shan, eastern margin of the Tibetan Plateau, from seismic reflection survey and finite element modelling: Journal of Geophysical Research: Solid Earth, v. 121, p. 767-787, https://doi.org/10.1002/2015JB012352.

Fleck, R. J., Sutter, J. F., and Elliot, D. H., 1997, Interpretation of discordant 40Ar/39Ar age-spectra of mesozoic tholeiites from antarctica: Geochimica Et Cosmochimica Acta, v. 41, no. 1, p. 15-32, https://doi.org/10.1016/0016-7037(77)90184-3.

Guo, X., Gao, R., Randy Keller, G., Xu, X., Wang, H., and Li, W., 2013, Imaging the crustal structure beneath the eastern Tibetan Plateau and implications for the uplift of the Longmen Shan range: Earth and Planetary Science Letters, v. 379, p. 72-80, https://doi.org/10.1016/j.epsl.2013.08.005.

Hames, W. E., and Burchfiel, B. C., 1993, Laser 40Ar/39Ar dating of Cenozoic, greenschist-facies shear zones, Longmen Shan, China: Geological Society of America, v. 25, no. 6, p. A-118, https://doi.org/10.1016/0012-821X(94)00079-4.

Harrison, T. M., 1992, Raising Tibet: Science, v. 255, no. 5052, p. 1663-1670, https://doi.org/doi: 10.1126/science.55.5052.1663.

Harrison, T. M., Célérier, J., Aikman, A. B., Hermann, J., and Heizler, M. T., 2009, Diffusion of 40Ar in muscovite: Geochimica Et Cosmochimica Acta, v. 73, no. 4, p. 1039-1051, https://doi.org/https://doi.org/10.1016/j.gca.2008.09.038.

1181 Harrowfield, M. J., and Wilson, C. J. L., 2005, Indosinian deformation of the Songpan
1182 Garze Fold Belt, northeast Tibetan Plateau: Journal of Structural Geology, v. 27,
1183 no. 1, p. 101-117, https://doi.org/10.1016/j.jsg.2004.06.010.
1184 Hu, J., Meng, Q., Shi, Y., and Qu, H., 2005, SHRIMP U-Pb dating of zircons from
1185 granitoid bodies in the Songpan-Ganzi terrane and its implications: Acta
1186 Petrologica Sinica, v. 21, no. 3, p. 867-880. (In Chinese with english abstract)
1187 Huang, M., Maas, R., Buick, I. S., and Williams, I. S., 2003a, Crustal response to
1188 continental collisions between the Tibet, Indian, South China and North China
1189 Blocks: geochronological constraints from the Songpan-Garzê Orogenic Belt,
1190 western China: Journal of Metamorphic Geology, v. 21, no. 3, p. 223-240,
1191 https://doi.org/10.1046/j.1525-1314.2003.00438.x.
1192 Huang, M. H., Buick, I. S., Hou, L. W., Huang, M. H., and Hou, L. W., 2003b,
1193 Tectonometamorphic evolution of the eastern Tibet plateau: Evidence from the
1194 central Songpan-Garze orogenic belt, western China: Journal of Petrology, v.
1195 44, no. 2, p. 255-278, https://doi.org/10.1093/petrology/44.2.255.
1196 Hubbard, J., and Shaw, J. H., 2009, Uplift of the Longmen Shan and Tibetan plateau,
1197 and the 2008 Wenchuan (M = 7.9) earthquake: Nature, v. 458, no. 7235, p. 194-
1198 197, https://doi.org/10.1038/nature07837.
1199 Jia, D., Wei, G., Chen, Z., Li, B., Zeng, Q., and Yang, G., 2006, Longmen Shan fold-
1200 thrust belt and its relation to the western Sichuan Basin in central China: New
1201 insights from hydrocarbon exploration: AAPG bulletin, v. 90, no. 9, p. 1425-
1202 1447, https://doi.org/10.1306/03230605076.
1203 Kirby, E., Reiners, P. W., Krol, M. A., Whipple, K. X., Hodges, K. V., Farley, K. A.,
1204 Tang, W., and Chen, Z., 2002, Late Cenozoic evolution of the eastern margin of
1205 the Tibetan Plateau: Inferences from 40Ar/39Ar and (U - Th)/He
1206 thermochronology: Tectonics, v. 21, no. 1, p. 1-1-1-20,
1207 https://doi.org/10.1029/2000TC001246.
1208 Kretz, R., 1983, Symbols for rock-forming minerals: Amer Miner, v. 68, no. 1, p. 277-
1209 279, https://doi.org/10.1016/0040-1951(84)90122-7.
1210 Lee, J.-Y., Marti, K., Severinghaus, J. P., Kawamura, K., Yoo, H.-S., Lee, J. B., and
1211 Kim, J. S., 2006, A redetermination of the isotopic abundances of atmospheric
1212 Ar: Geochimica et Cosmochimica Acta, v. 70, no. 17, p. 4507-4512,
1213 https://doi.org/10.1016/j.gca.2006.06.1563.

Li, H., Wang, H., Xu, Z., Si, J., Pei, J., Li, T., Huang, Y., Song, S.-R., Kuo, L.-W., Sun, Z., Chevalier, M.-L., and Liu, D., 2013a, Characteristics of the fault-related rocks, fault zones and the principal slip zone in the Wenchuan Earthquake Fault Scientific Drilling Project Hole-1 (WFSD-1): Tectonophysics, v. 584, p. 23-42, https://doi.org/10.1016/j.tecto.2012.08.021.

Li, H., Wang, H., Yang, G., Xu, Z., Li, T., Si, J., Sun, Z., Huang, Y., Chevalier, M.-L., Zhang, W., and Zhang, J., 2015, Lithological and structural characterization of the Longmen Shan fault belt from the 3rd hole of the Wenchuan Earthquake Fault Scientific Drilling project (WFSD-3): International Journal of Earth Sciences, https://doi.org/10.1007/s00531-015-1285-9.

Li, X. H., Liu, Y., Li, Q. L., Guo, C. H., and Chamberlain, K. R., 2009, Precise determination of Phanerozoic zircon Pb/Pb age by multicollector SIMS without external standardization: Geochemistry, Geophysics, Geosystems, v. 10, no. 4, https://doi.org/10.1029/2009gc002400.

Li, X. H., Tang, G. Q., Gong, B., Yang, Y. H., Hou, K. J., Hu, Z. C., Li, Q. L., Liu, Y., and Li, W. X., 2013b, Qinghu zircon: A working reference for microbeam analysis of U-Pb age and Hf and O isotopes: Chinese Science Bulletin, v. 58, no. 36, p. 4647-4654, https://doi.org/10.1007/s11434-013-5932-x.

Li, Y., Allen, P. A., Densmore, A. L., and Xu, Q., 2003, Evolution of the Longmen Shan foreland basin (western Sichuan, China) during the Late Triassic Indosinian orogeny: Basin Research, v. 15, no. 1, p. 117-138, https://doi.org/10.1046/j.1365-2117.2003.00197.x.

Li, Y., Su, D., Zhou, R., Li, H., Densmore, A. L., Yan, L., and Yan, Z., 2013c, Episodic orogeny deduced from coeval sedimentary sequences in the foreland basin and its implication for uplift process of Longmen Mountain, China: Journal of Mountain Science, v. 10, no. 1, p. 29-42, https://doi.org/10.1007/s11629-013-2238-z.

Li, Z., 2009, Composition, structural characteristics and evolution of back-Longmenshan orogen (north section) in the northwest margin of Yangtze block [Doctoral thesis: Chang'an University, 211 p.

Lin, A., Rao, G., and Yan, B., 2014, Structural analysis of the right-lateral strike-slip Qingchuan fault, northeastern segment of the Longmen Shan thrust belt, central China: Journal of Structural Geology, v. 68, p. 227-244,

https://doi.org/10.1016/j.jsg.2014.09.014.

Liu, H., Yan, D., and Wei, G., 2008, Deformation and metamorphism sequence of bikou terrane in the northwest margin of yangtze plate：implications for extension collapse and transition of songpan—garze orogenic belt: Acta Geologica Sinica, no. 04, p. 464-474+578-579. (In Chinese with english abstract)

Long, X., 1991, Several questions of geochronic evolution in the mid-northeast segment of lLongmenshan Mountains: Journal of Chengdu College of geology, v. 18, no. 1, p. 8-16. (In Chinese with english abstract)

Lovera, O. M., Richter, F. M., and Harrison, T. M., 1989, 40Ar/39Ar geothermometry for slowly cooled samples having a distribution of diffusion domain size: Journal of Geophysical Research, v. 94, no. 17, p. 917-936, https://doi.org/10.1029/JB094iB12p17917.

Ludwig, K. R., 2003, User's manual for Isoplot 3.00: a geochronological toolkit for Microsoft Excel: Berkeley Geochrongol. Center Special Publication, v. 4, p. 47–93.

Luo, Z., 1991, The dynamical model of the lithospheric evolution in Longmenshan Orogenic Belt: Journal of Chengdu College of geology, no. 1, p. 1-7. (In Chinese with english abstract)

Ma, Y., Wang, G., and Hu, X., 1996, Tectonic deformation of Pengguan complex: Acta Geologica Sichuan, no. 02, p. 110-114. (In Chinese with english abstract)

Mattauer, M., Malavieille, J., Calassou, S., Lancelot, J., Roger, R., Hao, Z., Xu, Z. Q., and Hou, L. W., 1992, Le chaine Triassique de Songpan-Garze (Ouest Sichuan et est Tibet): Une chaine de plissement-decollement sur marge passive: Comptes Rendus de L'Academie Des Sciences, p. 619-626.

McDougall, I., and Harrison, T. M., 1988, Geochronology and thermo- chronology by the 40Ar/39Ar method, New York, Oxford University Press.

Meng, Q.-R., Wang, E., and Hu, J.-M., 2005, Mesozoic sedimentary evolution of the northwest Sichuan basin: Implication for continued clockwise rotation of the South China block: Geological Society of America Bulletin, v. 117, no. 3-4, p. 396-410, https://doi.org/10.1130/B25407.1.

Paterson, S. R., Tobisch, O. T., and Bhattacharyya, T., 1989, Regional, structural and strain analyses of terranes in the Western Metamorphic Belt, Central Sierra Nevada, California: Journal of structural geology, v. 11, no. 3, p. 255-273,

https://doi.org/10.1016/0191-8141(89)90066-7.

Phillips, D., Matchan, E. L., Honda, M., and Kuiper, K. F., 2017, Astronomical calibration of 40 Ar/ 39 Ar reference minerals using high-precision, multi-collector (ARGUSVI) mass spectrometry: Geochimica et Cosmochimica Acta, v. 196, p. 351-369, https://doi.org/10.1016/j.gca.2016.09.027.

Richardson, N. J., Densmore, A. L., Seward, D., Fowler, A., Wipf, M., Ellis, M. A., Yong, L., and Zhang, Y., 2008, Extraordinary denudation in the Sichuan Basin: Insights from low-temperature thermochronology adjacent to the eastern margin of the Tibetan Plateau: Journal of Geophysical Research, v. 113, no. B4, https://doi.org/10.1029/2006jb004739.

Robert, A., Pubellier, M., De Sigoyer, J., Vergne, J., Lahfid, A., Cattin, R., Findling, N., and Zhu, J., 2010a, Structural and thermal characters of the Longmen Shan (Sichuan, China): tectonophysics, v. 491, no. 1, p. 165-173, https://doi.org/10.1016/j.tecto.2010.03.018.

Robert, A., Zhu, J., Vergne, J., Cattin, R., Chan, L. S., Wittlinger, G., Herquel, G., de Sigoyer, J., Pubellier, M., and Zhu, L. D., 2010b, Crustal structures in the area of the 2008 Sichuan earthquake from seismologic and gravimetric data: Tectonophysics, v. 491, no. 1-4, p. 205-210, https://doi.org/10.1016/j.tecto.2009.11.010.

Roger, F., Jolivet, M., Cattin, R., and Malavieille, J., 2011, Mesozoic-Cenozoic tectonothermal evolution of the eastern part of the Tibetan Plateau (Songpan-Garze, Longmen Shan area): insights from thermochronological data and simple thermal modelling: Geological Society, London, Special Publications, v. 353, no. 1, p. 9-25, https://doi.org/10.1144/sp353.2.

Roger, F., Malavieille, J., Leloup, P. H., Calassou, S., and Xu, Z., 2004, Timing of granite emplacement and cooling in the Songpan–Garzê Fold Belt (eastern Tibetan Plateau) with tectonic implications: Journal of Asian Earth Sciences, v. 22, no. 5, p. 465-481, https://doi.org/10.1016/s1367-9120(03)00089-0.

Royden, L. H., Burchfiel, B. C., and van der Hilst, R. D., 2008, The geological evolution of the Tibetan Plateau: science, v. 321, no. 5892, p. 1054-1058, https://doi.org/10.1126/science.1155371.

Sengör, A. M. C., 1984, The Cimmeride Orogenic System and the Tectonics of Eurasia: Geological Society of America Special Papers, v. 195, p. 1-74,

https://doi.org/10.1130/SPE195-p1.

Shen, Z.-K., Sun, J., Zhang, P., Wan, Y., Wang, M., Bürgmann, R., Zeng, Y., Gan, W., Liao, H., and Wang, Q., 2009, Slip maxima at fault junctions and rupturing of barriers during the 2008 Wenchuan earthquake: Nature Geoscience, v. 2, no. 10, p. 718-724, https://doi.org/10.1038/ngeo636.

Sláma, J., Košler, J., Condon, D. J., Crowley, J. L., Gerdes, A., Hanchar, J. M., Horstwood, M. S. A., Morris, G. A., Nasdala, L., Norberg, N., Schaltegger, U., Schoene, B., Tubrett, M. N., and Whitehouse, M. J., 2008, Plešovice zircon — A new natural reference material for U–Pb and Hf isotopic microanalysis: Chemical Geology, v. 249, no. 1, p. 1-35, https://doi.org/10.1016/j.chemgeo.2007.11.005.

Stacey, J. S., and Kramers, J. D., 1975, Approximation of terrestrial lead isotope evolution by a two-stage model: Earth and Planetary Science Letters, v. 26, no. 2, p. 207-221, https://doi.org/10.1016/0012-821X(75)90088-6.

Tian, Y., Kohn, B. P., Phillips, D., Hu, S., Gleadow, A. J., and Carter, A., 2016, Late Cretaceous–earliest Paleogene deformation in the Longmen Shan fold-and-thrust belt, eastern Tibetan Plateau margin: Pre-Cenozoic thickened crust?: Tectonics, p. 1-20, https://doi.org/10.1002/2016TC004182.

Wallis, S. R., Tsujimori, T., Aoya, M., Kawakami, T., Terada, K., Suzuki, K., and Hyodo, H., Cenozoic and Mesozoic metamorphism in the Longmenshan orogen: Implications for geodynamic models of eastern Tibet, *in* Proceedings AGU Fall Meeting Abstracts2003, p. 745-748.

Wang, E., Kirby, E., Furlong, K. P., van Soest, M., Xu, G., Shi, X., Kamp, P. J. J., and Hodges, K. V., 2012a, Two-phase growth of high topography in eastern Tibet during the Cenozoic: Nature Geosci, v. 5, no. 9, p. 640-645, https://doi.org/10.1038/ngeo1538.

Wang, E., Meng, K., Chu, J. J., Wang, G., and Chen, Z., East Tibet Detachment: Evidence for the uplift mechanism of the Longmen Shan fault belt2012b.

Wang, Q., Liang, B., Xie, Q., and He, W., 2000, Research on microstructures and deformation conditions of the Qingchuan fault zone: Journal of Mineral Petrology, v. 87, no. 01, p. 87-90. (In Chinese with english abstract)

Wei, C., 1994, Metamorphism and its geological significance of the Bikou Group in the Shanxi–Gansu–Sichuan border region: Acta Geologica Sinica, v. 68, no. 03, p.

241-254. (In Chinese with english abstract)

Weislogel, A. L., Graham, S. A., Chang, E. Z., Wooden, J. L., and Gehrels, G. E., 2010, Detrital zircon provenance from three turbidite depocenters of the Middle-Upper Triassic Songpan-Ganzi complex, central China: Record of collisional tectonics, erosional exhumation, and sediment production: Geological Society of America Bulletin, v. 122, no. 11-12, p. 2041-2062, https://doi.org/10.1130/b26606.1.

Weller, O. M., St-Onge, M. R., Waters, D. J., Rayner, N., Searle, M. P., Chung, S. L., Palin, R. M., Lee, Y. H., and Xu, X., 2013, Quantifying Barrovian metamorphism in the Danba Structural Culmination of eastern Tibet: Journal of Metamorphic Geology, v. 31, no. 9, p. 909-935, https://doi.org/10.1111/jmg.12050.

West, D. P., and Lux, D. R., 1993, Dating mylonitic deformation by the 40Ar-39Ar method: An example from the Norumbega Fault Zone, Maine: Earth and Planetary Science Letters, v. 120, no. 3-4, p. 221-237, https://doi.org/10.1016/0012-821X(93)90241-Z.

Worley, B. A., and Wilson, C. J., 1996, Deformation partitioning and foliation reactivation during transpressional orogenesis, an example from the Central Longmen Shan, China: Journal of Structural Geology, v. 18, no. 4, p. 395-411, https://doi.org/10.1016/0191-8141(95)00095-U.

Xia, Z., 1993, Syntectonic regional epimetamorphism of the Triassic terrigenous detrital rocks in the Songpan-Ganze orogneic belt during the early Yanshanian orogney: Acta Geologica Sichuan, no. 03, p. 189-192. (In Chinese with english abstract)

Xu, C., Wells, M. L., Yan, D.-P., Qiu, L., Zhou, Y., and Zhang, Y., 2020, Phase equilibria and geochronology of Triassic blueschists in the Bikou terrane and Mesozoic tectonic evolution of the northwestern margin of the Yangtze Block (SW China): Journal of Asian Earth Sciences, v. 201, p. 104513, https://doi.org/https://doi.org/10.1016/j.jseaes.2020.104513.

Xu, Z., Hou, L., and Wang, Z., 1992, Orogenic process of the Songpan-Ganzé Orogenic belt of China., Geological Publishing House, Beijing, 1-189 p.:

Xu, Z., Ji, S., Li, H., Hou, L., Fu, X., and Cai, Z., 2008, Uplift of the Longmen Shan range and the Wenchuan earthquake: Episodes, v. 31, no. 3, p. 291-301,

https://doi.org/10.1007/s00254-008-1393-y.

Xue, Z., Martelet, G., Lin, W., Faure, M., Chen, Y., Wei, W., Li, S., and Wang, Q., 2017, Mesozoic crustal thickening of the Longmenshan belt (NE Tibet, China) by imbrication of basement slices: insights from structural analysis, petrofabric and magnetic fabric studies, and gravity modeling: Tectonics, p. 3110-3134, https://doi.org/10.1002/2017TC004754.

Xue, Z., Shang, Q., Jiang, W., Wang, Q., and Li, S., 2016, Emplacement age and tectonic implications of the brecciated limestone at the edge of the Longmenshan klippe: Science China Earth Sciences, v. 59, no. 3, p. 590-600, https://doi.org/10.1007/s11430-015-5209-0.

Yan, D., Zhou, M., Li, S., and Wei, G., 2011, Structural and geochronological constraints on the Mesozoic-Cenozoic tectonic evolution of the Longmen Shan thrust belt, eastern Tibetan Plateau: Tectonics, v. 30, no. 6, p. 1-24, https://doi.org/10.1029/2011TC002867.

Yan, D., Zhou, M., Wei, G., Gao, J., Liu, S., Xu, P., and Shi, X., 2008, The Pengguan tectonic dome of Longmen Mountains, Sichuan Province: Mesozoic denudation of a Neoproterozoic magmatic arc-basin system: Science in China Series D: Earth Sciences, v. 51, no. 11, p. 1545-1559, https://doi.org/10.1007/s11430-008-0126-0.

Yan, D.-P., Qiu, L., Wells, M. L., Zhou, M.-F., Meng, X., Lu, S., Zhang, S., Wang, Y., and Li, S.-B., 2018, Structural and Geochronological Constraints on the Early Mesozoic North Longmen Shan Thrust Belt: Foreland Fold-Thrust Propagation of the SW Qinling Orogenic Belt, Northeastern Tibetan Plateau: Tectonics, v. 37, no. 12, p. 4595-4624, https://doi.org/10.1029/2018tc004986.

Yan, Q., Wang, Z., Hanson, A., Druschke, P., Yan, Z., Liu, D., Jian, P., Song, B., Wang, T., and Jiang, C., 2003, SHRIMP age and geochemistry of the Bikou volcanic terrane: implications for Neoproterozoic tectonics on the northern margin of the Yangtze Craton: Acta Geologica Sinica (English Edition), v. 77, no. 4, p. 479-490.

Yan, Z., Tian, Y., Li, R., Vermeesch, P., Sun, X., Li, Y., Rittner, M., Carter, A., Shao, C., Huang, H., and Ji, X., 2019, Late Triassic tectonic inversion in the upper Yangtze Block: Insights from detrital zircon U–Pb geochronology from south-western Sichuan Basin: Basin Research, v. 31, no. 1, p. 92-113,

https://doi.org/https://doi.org/10.1111/bre.12310.

Yin, A., The Songpan-ganzi terrane of Tibet: was it a part of South China since the Neopreoterozoic, *in* Proceedings 2015 GSA Annual Meeting in Baltimore, Maryland, USA, 2015, Volume 47, Geological Society of America, p. 38.

Yin, A., and Nie, S., 1993, An indentation model for the North and South China collision and the development of the Tan-Lu and Honam fault systems, Eastern Asia: Tectonics, v. 12, no. 4, p. 801-813.

Yuan, C., Zhou, M.-F., Sun, M., Zhao, Y., Wilde, S., Long, X., and Yan, D., 2010, Triassic granitoids in the eastern Songpan Ganzi Fold Belt, SW China: Magmatic response to geodynamics of the deep lithosphere: Earth and Planetary Science Letters, v. 290, no. 3-4, p. 481-492, https://doi.org/10.1016/j.epsl.2010.01.005.

Yuan, H., Zhang, Z., and Zhang, P., 1991, The uplift and cooling histories of Laojungou granite in the western margin of the central Longmen Mountain: Journal of Chengdu College of geology, v. 18, no. 1, p. 17-22. (In Chinese with english abstract)

Zhang, H., Parrish, R., Zhang, L., Xu, W., Yuan, H., Gao, S., and Crowley, Q. G., 2007, A-type granite and adakitic magmatism association in Songpan–Garze fold belt, eastern Tibetan Plateau: Implication for lithospheric delamination: Lithos, v. 97, no. 3-4, p. 323-335, https://doi.org/10.1016/j.lithos.2007.01.002.

Zhang, H., Zhang, L., Harris, N., Jin, L., and Yuan, H., 2006a, U–Pb zircon ages, geochemical and isotopic compositions of granitoids in Songpan-Garze fold belt, eastern Tibetan Plateau: constraints on petrogenesis and tectonic evolution of the basement: Contributions to Mineralogy and Petrology, v. 152, no. 1, p. 75-88, https://doi.org/10.1007/s00410-006-0095-2.

Zhang, H.-P., Liu, S.-F., Yang, N., Zhang, Y.-Q., and Zhang, G.-W., 2006b, Geomorphic characteristics of the Minjiang drainage basin (eastern Tibetan Plateau) and its tectonic implications: New insights from a digital elevation model study: The Island Arc, v. 15, no. 2, p. 239-250, https://doi.org/10.1111/j.1440-1738.2006.00524.x.

Zhang, K.-J., Li, B., Wei, Q.-G., Cai, J.-X., and Zhang, Y.-X., 2008, Proximal provenance of the western Songpan–Ganzi turbidite complex (Late Triassic, eastern Tibetan plateau): Implications for the tectonic amalgamation of China:

1445 Sedimentary Geology, v. 208, no. 1-2, p. 36-44,
1446 https://doi.org/10.1016/j.sedgeo.2008.04.008.
1447 Zhang, P., Shen, Z., Wang, M., Gan, W., Bürgmann, R., Molnar, P., Wang, Q., Niu, Z.,
1448 Sun, J., Wu, J., Hanrong, S., and Xinzhao, Y., 2004, Continuous deformation of
1449 the Tibetan Plateau from global positioning system data: Geology, v. 32, no. 9,
1450 p. 809, https://doi.org/10.1130/g20554.1.
1451 Zhang, Y. X., Li, B., Wei, Q. G., Wang, Y., and Zhang, K. J., 2006c, Detrital zircon
1452 provenance of the Late Triassic Songpan-Ganzi complex: Sedimentary record
1453 of collision of the North and South China blocks: Comment and Reply:
1454 COMMENT: Geology, v. 34, no. 1, p. e107-e107,
1455 https://doi.org/10.1130/g22944.1.
1456 Zhang, Z., Wang, Y., Chen, Y., Houseman, G. A., Tian, X., Wang, E., and Teng, J., 2009,
1457 Crustal structure across Longmenshan fault belt from passive source seismic
1458 profiling: Geophysical Research Letters, v. 36, no. 17, p. L17310-,
1459 https://doi.org/10.1029/2009gl039580.
1460 Zhang, Z., Yuan, X., Chen, Y., Tian, X., Kind, R., Li, X., and Teng, J., 2010, Seismic
1461 signature of the collision between the east Tibetan escape flow and the Sichuan
1462 Basin: Earth and Planetary Science Letters, v. 292, no. 3-4, p. 254-264,
1463 https://doi.org/10.1016/j.epsl.2010.01.046.
1464 Zhao, Y., 2007, Mesozoic granitoids in Eastern Songpan-Garze: Geochemistry,
1465 petrogenesis and tectonic implications [Doctor: Graduate school of the Chinese
1466 Academy of Sciences, 111 p.
1467 Zheng, Y., Kong, P., and Fu, B., 2014, Time constraints on the emplacement of klippen
1468 in the Longmen Shan thrust belt and tectonic implications: Tectonophysics, v.
1469 634, p. 44-54, https://doi.org/10.1016/j.tecto.2014.07.018.
1470 Zheng, Y., Li, H., Sun, Z., Wang, H., Zhang, J., Li, C., and Cao, Y., 2016, New
1471 geochronology constraints on timing and depth of the ancient earthquakes along
1472 the Longmen Shan fault belt, eastern Tibet: Tectonics, v. 35, no. 12, p. 2781-
1473 2806, https://doi.org/10.1002/2016TC004210.
1474 Zhou, M., Yan, D., Kennedy, A. K., Li, Y., and Ding, J., 2002, SHRIMP U–Pb zircon
1475 geochronological and geochemical evidence for Neoproterozoic arc-
1476 magmatism along the western margin of the Yangtze Block, South China: Earth
1477 and Planetary Science Letters, v. 196, no. 1, p. 51-67,

https://doi.org/10.1016/S0012-821X(01)00595-7.

Zhou, M., Yan, D., Vasconcelos, P. M., Li, J., and Hu, R., 2008, Structural and geochronological constraints on the tectono-thermal evolution of the Danba domal terrane, eastern margin of the Tibetan plateau: Journal of Asian Earth Sciences, v. 33, no. 5, p. 414-427, https://doi.org/10.1002/2016TC004210.

Figure 1

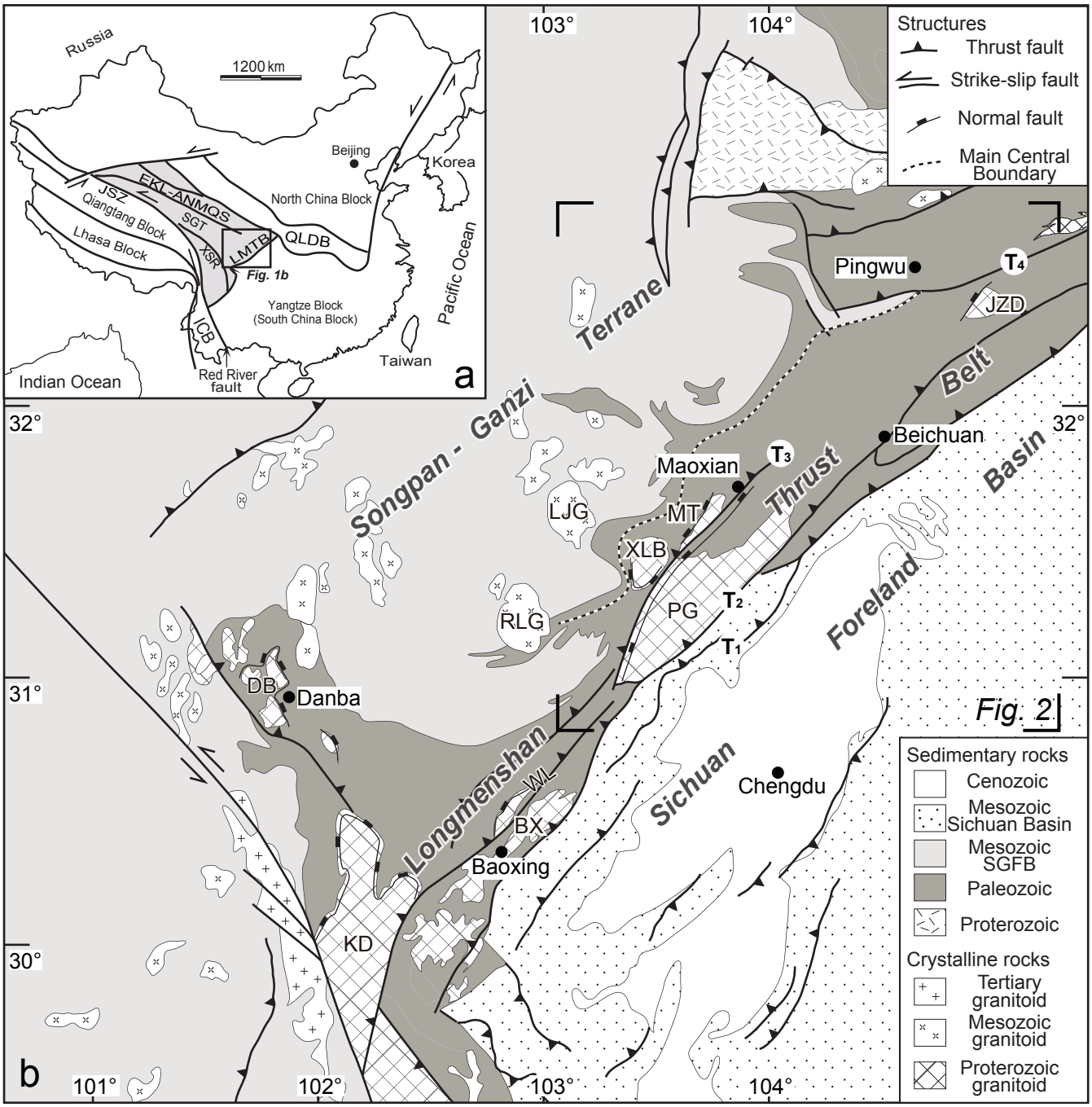
Russia
1200 km
Beijing
Korea
North China Block
JSZ
EKL-ANMQS
Qiangtang Block
SGT
Lhasa Block
YSR
LMTB
QLDB
Fig. 1b
Yangtze Block
(South China Block)
Pacific Ocean
ICB
Taiwan
Indian Ocean
Red River
fault
a
103°
104°
Structures
Thrust fault
Strike-slip fault
Normal fault
Main Central
Boundary
Terrane
Pingwu
T4
JZD
Belt
Songpan - Ganzi
32°
Beichuan
Basin
Maoxian
T3
Thrust
LJG
MT
XLB
PG
T2
T1
RLG
Foreland
Fig. 2
31°
DB
Danba
Longmenshan
WL
BX
Baoxing
Sichuan
Chengdu
KD
30°
b
101°
102°
103°
104°
Sedimentary rocks
Cenozoic
Mesozoic
Sichuan Basin
Mesozoic
SGFB
Paleozoic
Proterozoic
Crystalline rocks
Tertiary
granitoid
Mesozoic
granitoid
Proterozoic
granitoid

Figure 2

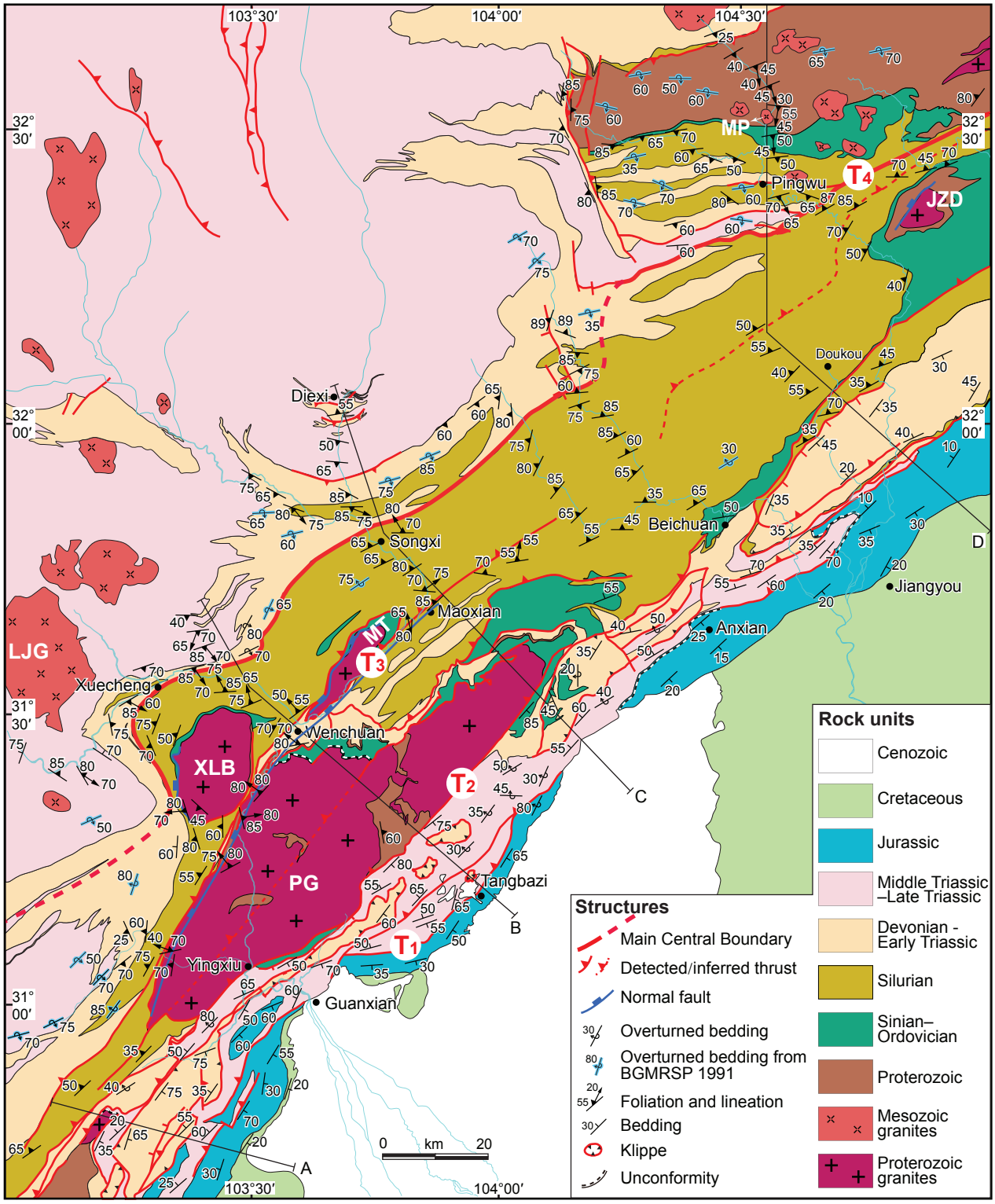
103°30′
104°00′
104°30′
32° 30′
32° 00′
31° 30′
31° 00′
MP
T4
JZD
Pingwu
Doukou
Diexi
Songxi
Beichuan
Jiangyou
Maoxian
Anxian
MT
T3
LJG
Xuecheng
Wenchuan
XLB
T2
PG
Tangbazi
T1
Yingxiu
Guanxian
A
B
C
D
0 km 20
Rock units
Cenozoic
Cretaceous
Jurassic
Middle Triassic –Late Triassic
Devonian - Early Triassic
Silurian
Sinian– Ordovician
Proterozoic
Mesozoic granites
Proterozoic granites
Structures
Main Central Boundary
Detected/inferred thrust
Normal fault
Overturned bedding
Overturned bedding from BGMRSP 1991
Foliation and lineation
Bedding
Klippe
Unconformity

Figure 3

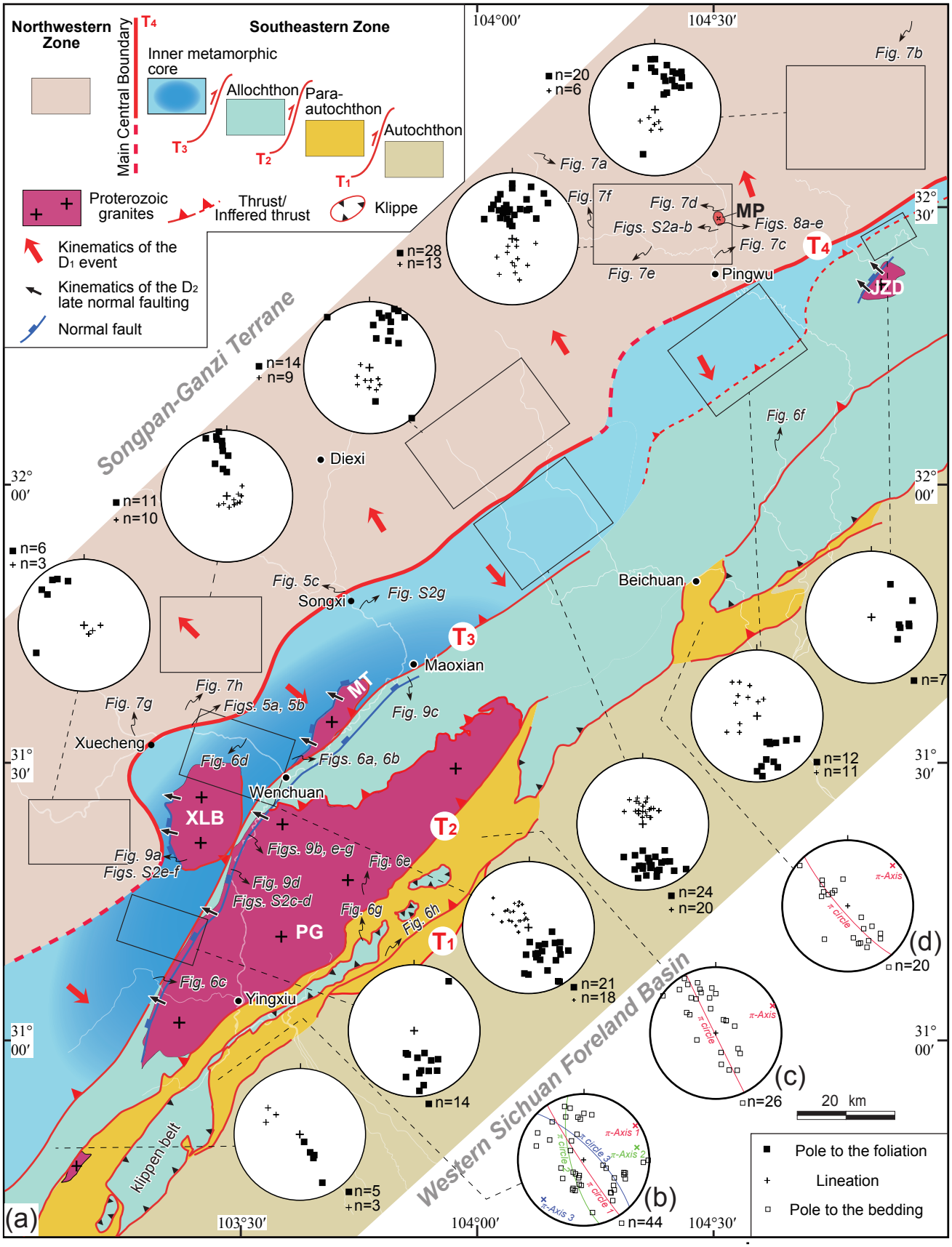
Northwestern Zone
Southeastern Zone
Main Central Boundary
T4
T3
T2
T1
Inner metamorphic core
Allochthon
Para-autochthon
Autochthon
Proterozoic granites
Thrust/ Inffered thrust
Klippe
Kinematics of the D1 event
Kinematics of the D2 late normal faulting
Normal fault
Songpan-Ganzi Terrane
Western Sichuan Foreland Basin
104°00′
104°30′
103°30′
32° 00′
31° 30′
31° 00′
Fig. 7b
Fig. 7a
Fig. 7f
Fig. 7d
Fig. 7e
Fig. 7c
Figs. S2a-b
Figs. 8a-e
MP
Pingwu
JZD
Fig. 6f
Diexi
Fig. 5c
Songxi
Fig. S2g
Beichuan
Fig. 7h
Figs. 5a, 5b
Fig. 7g
MT
Fig. 9c
Maoxian
Xuecheng
Fig. 6d
Figs. 6a, 6b
Wenchuan
XLB
Fig. 9a
Figs. S2e-f
Figs. 9b, e-g
Fig. 6e
Fig. 9d
Figs. S2c-d
Fig. 6g
Fig. 6h
PG
Fig. 6c
Yingxiu
Klippen belt
n=20
n=6
n=28
n=13
n=14
n=9
n=11
n=10
n=6
n=3
n=7
n=12
n=11
n=24
n=20
n=21
n=18
n=14
n=5
n=3
n=44
n=26
n=20
(a)
(b)
(c)
(d)
π-Axis
π circle
20 km
Pole to the foliation
Lineation
Pole to the bedding

Figure 4

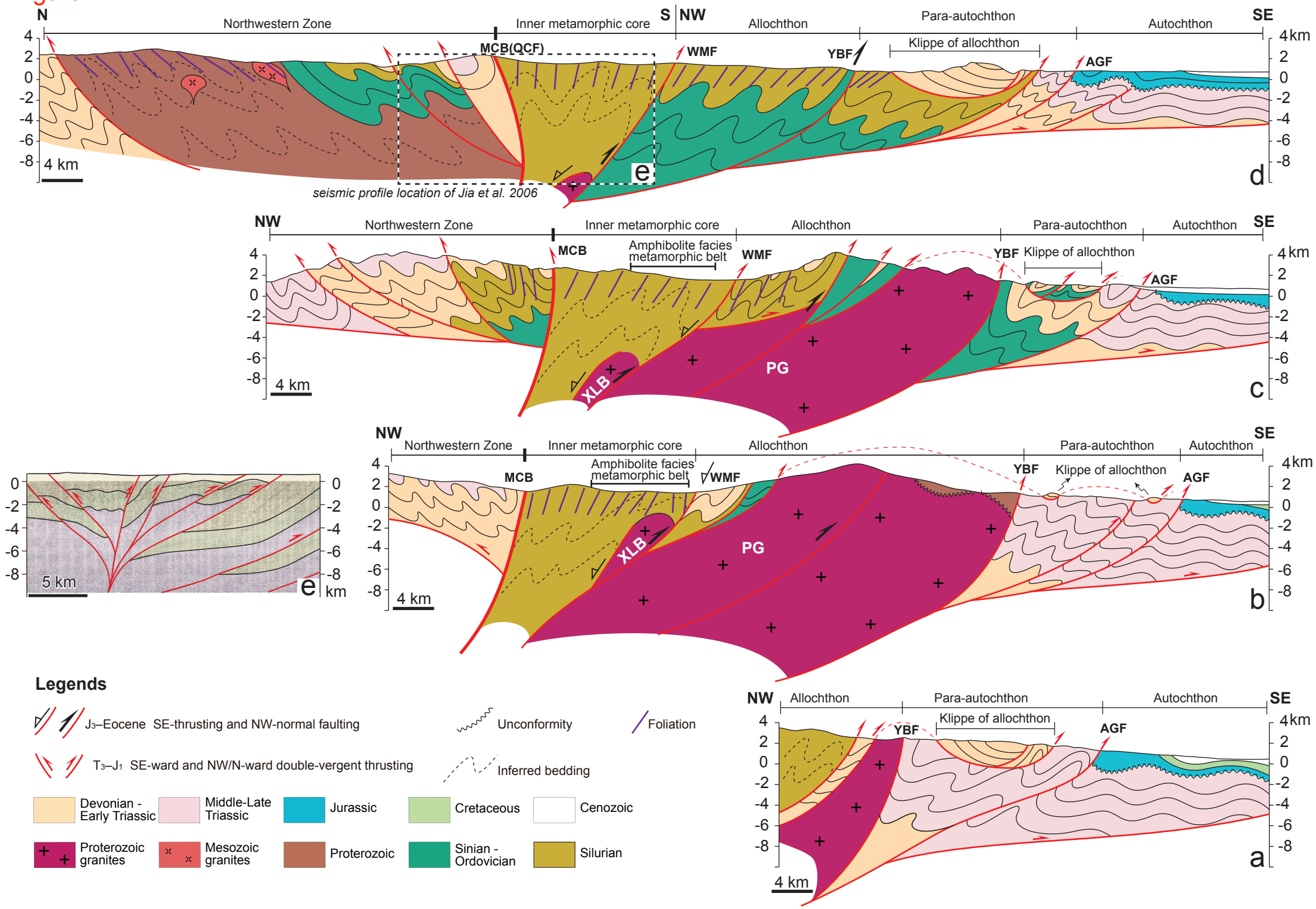
N
Northwestern Zone
Inner metamorphic core
S
NW
Allochthon
Para-autochthon
Autochthon
SE
MCB(QCF)
WMF
YBF
Klippe of allochthon
AGF
4 km
e
d
seismic profile location of Jia et al. 2006
NW
Northwestern Zone
Inner metamorphic core
Allochthon
Para-autochthon
Autochthon
SE
MCB
Amphibolite facies metamorphic belt
WMF
YBF
Klippe of allochthon
AGF
PG
XLB
4 km
c
NW
Northwestern Zone
Inner metamorphic core
Allochthon
Para-autochthon
Autochthon
SE
MCB
Amphibolite facies metamorphic belt
WMF
YBF
Klippe of allochthon
AGF
PG
XLB
4 km
b
5 km
e
km
NW
Allochthon
Para-autochthon
Autochthon
SE
YBF
Klippe of allochthon
AGF
4 km
a
Legends
J3–Eocene SE-thrusting and NW-normal faulting
T3–J1 SE-ward and NW/N-ward double-vergent thrusting
Unconformity
Inferred bedding
Foliation
Devonian - Early Triassic
Middle-Late Triassic
Jurassic
Cretaceous
Cenozoic
Proterozoic granites
Mesozoic granites
Proterozoic
Sinian - Ordovician
Silurian

Figure 5

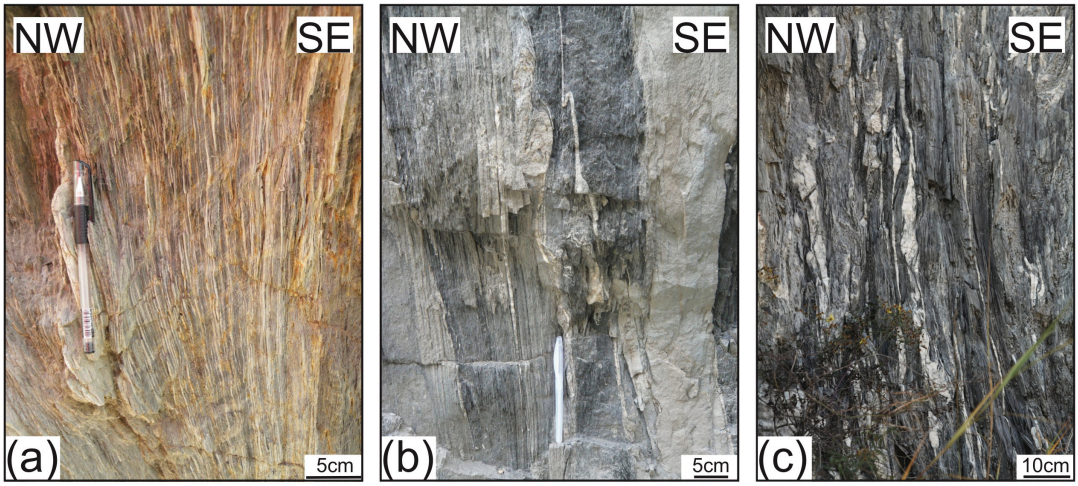

Figure 6

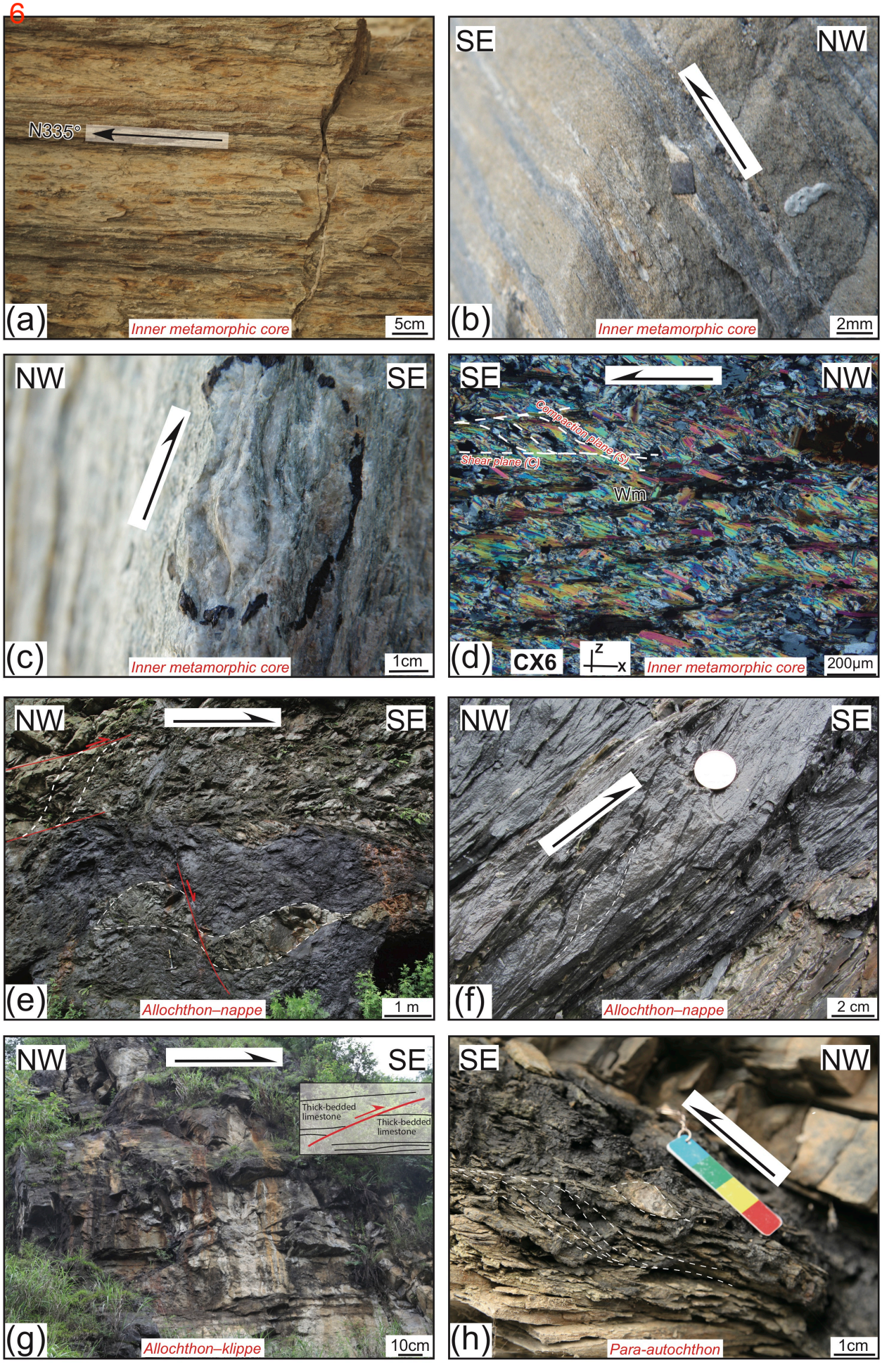
N335°
(a)
Inner metamorphic core
5cm
SE
NW
(b)
Inner metamorphic core
2mm
NW
SE
(c)
Inner metamorphic core
1cm
SE
NW
Compaction plane (S)
Shear plane (C)
Wm
(d)
cx6
z
x
Inner metamorphic core
200µm
NW
SE
(e)
Allochthon–nappe
1 m
NW
SE
(f)
Allochthon–nappe
2 cm
NW
SE
Thick-bedded limestone
Thick-bedded limestone
(g)
Allochthon–klippe
10cm
SE
NW
(h)
Para-autochthon
1cm

Figure 7

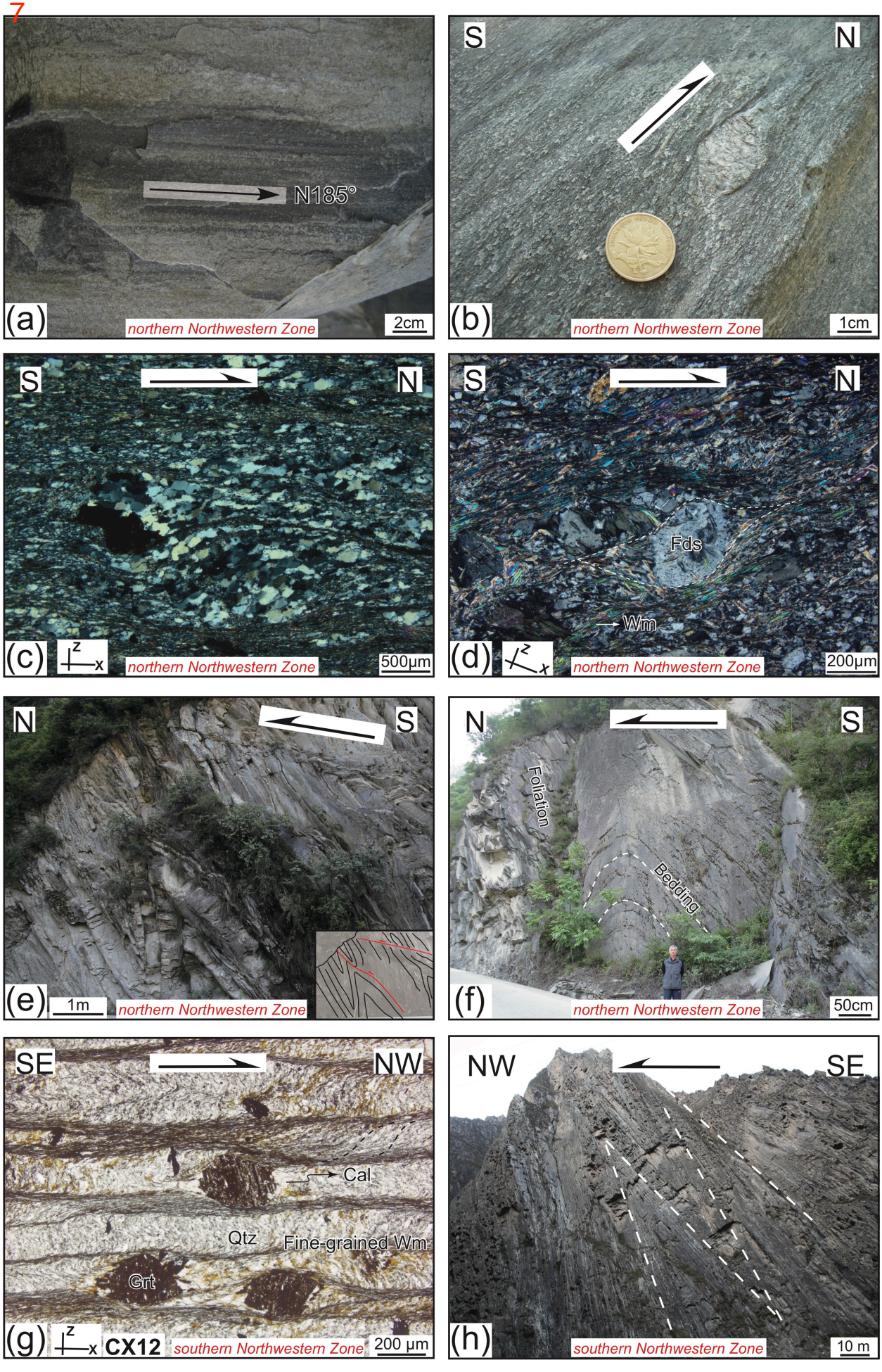
N185°
(a)
northern Northwestern Zone
2cm
S
N
(b)
northern Northwestern Zone
1cm
S
N
(c)
z
x
northern Northwestern Zone
500μm
S
N
Fds
Wm
(d)
z
x
northern Northwestern Zone
200μm
N
S
(e)
1m
northern Northwestern Zone
N
S
Foliation
Bedding
(f)
northern Northwestern Zone
50cm
SE
NW
Cal
Qtz
Fine-grained Wm
Grt
(g)
z
x
CX12
southern Northwestern Zone
200 μm
NW
SE
(h)
southern Northwestern Zone
10 m

Figure 8

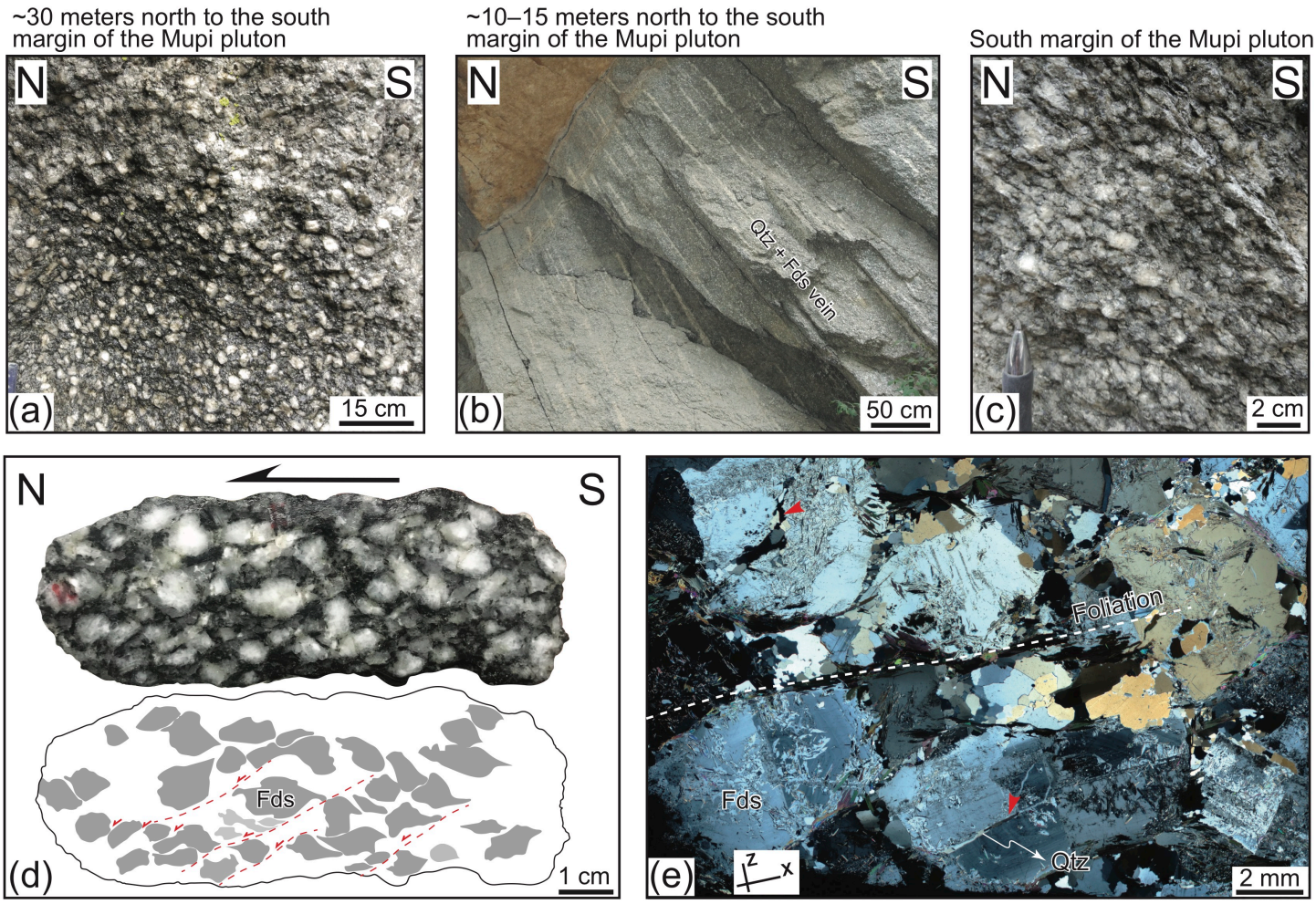
~30 meters north to the south margin of the Mupi pluton
~10–15 meters north to the south margin of the Mupi pluton
South margin of the Mupi pluton
N
S
(a)
15 cm
Qtz + Fds vein
(b)
50 cm
(c)
2 cm
Fds
(d)
1 cm
Foliation
Fds
Qtz
(e)
2 mm

Figure 9

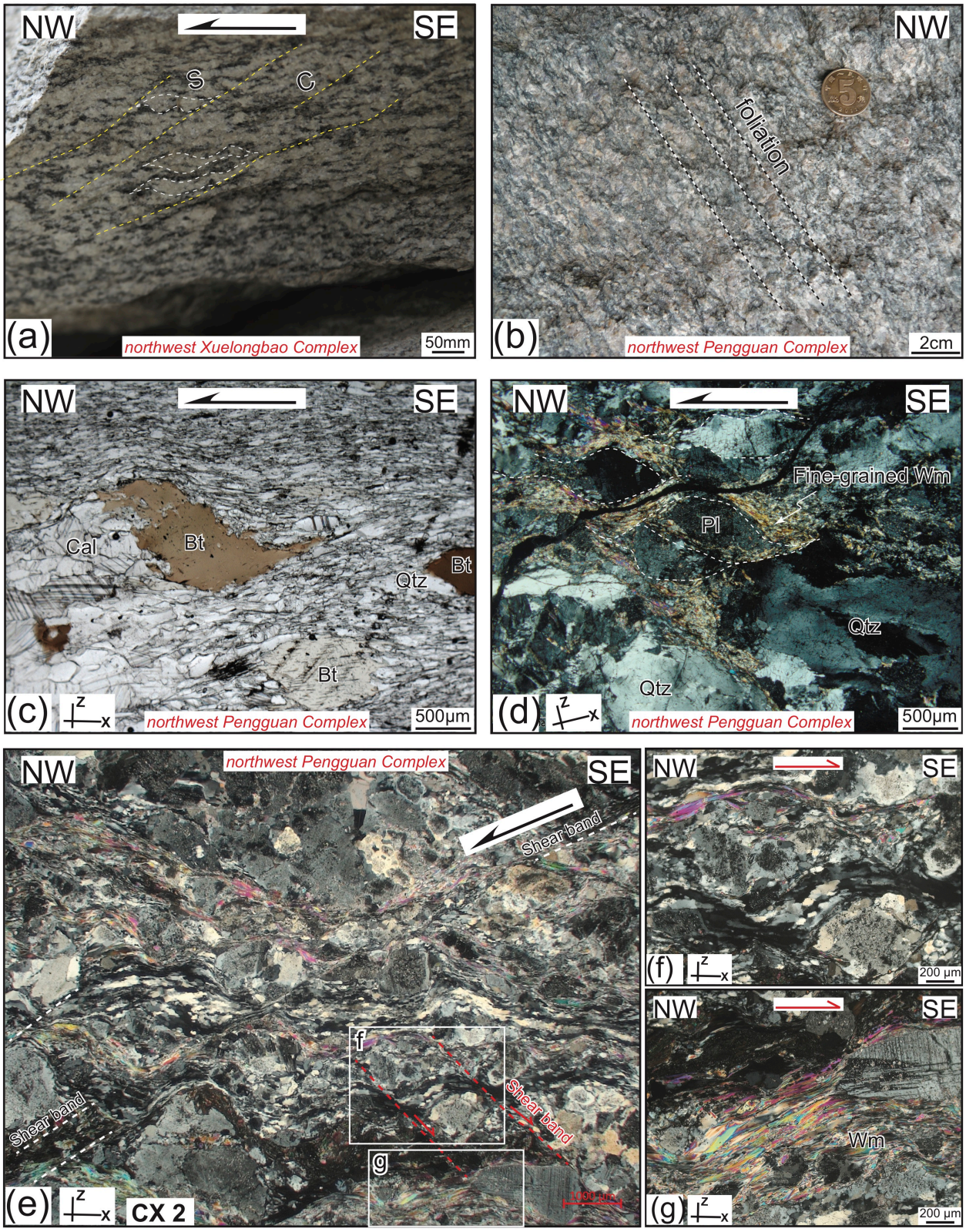
NW
SE
S
C
(a)
northwest Xuelongbao Complex
50mm
NW
foliation
(b)
northwest Pengguan Complex
2cm
NW
SE
Cal
Bt
Bt
Qtz
Bt
(c)
northwest Pengguan Complex
500μm
NW
SE
Fine-grained Wm
Pl
Qtz
Qtz
(d)
northwest Pengguan Complex
500μm
NW
northwest Pengguan Complex
SE
Shear band
f
g
Shear band
Shear band
(e)
cx 2
NW
SE
(f)
200 μm
NW
SE
Wm
(g)
200 μm

Figure 10

Northwestern Zone

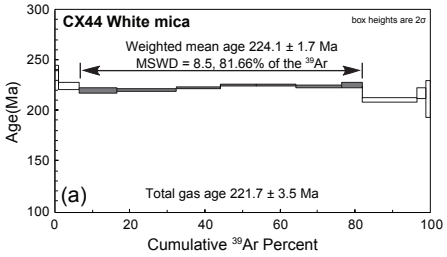

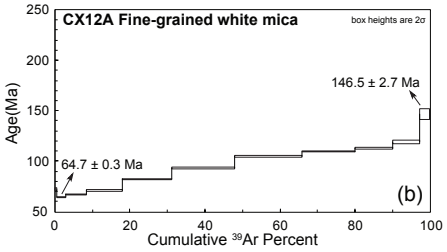

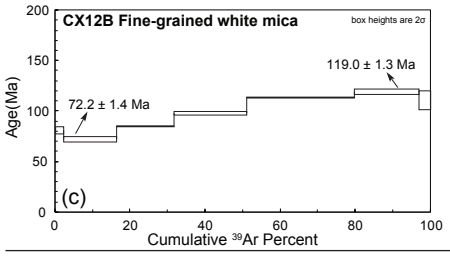

Southeastern Zone -- *Inner metamorphic core*

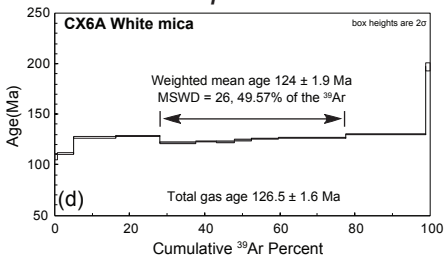

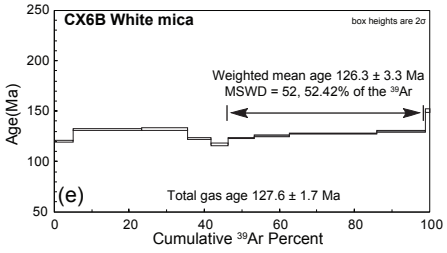

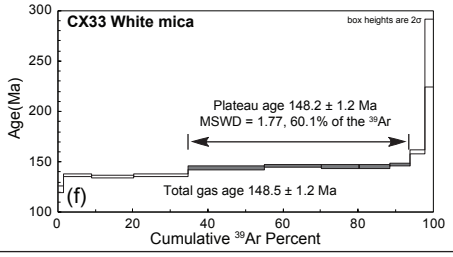

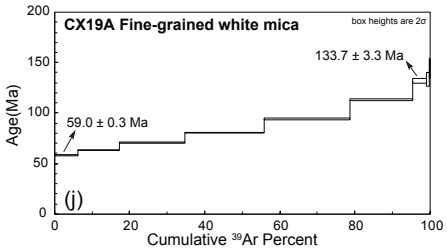

Basement Complex

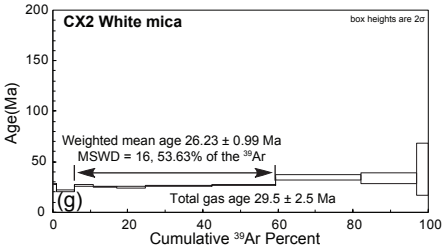

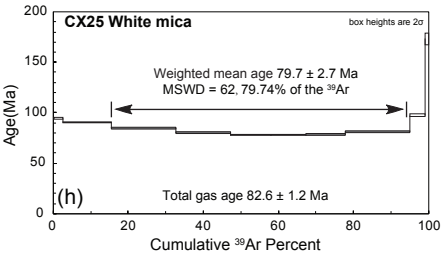

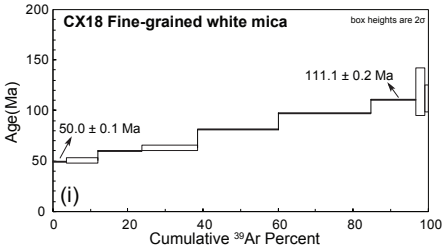

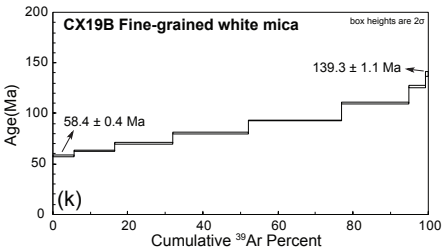

Figure 11

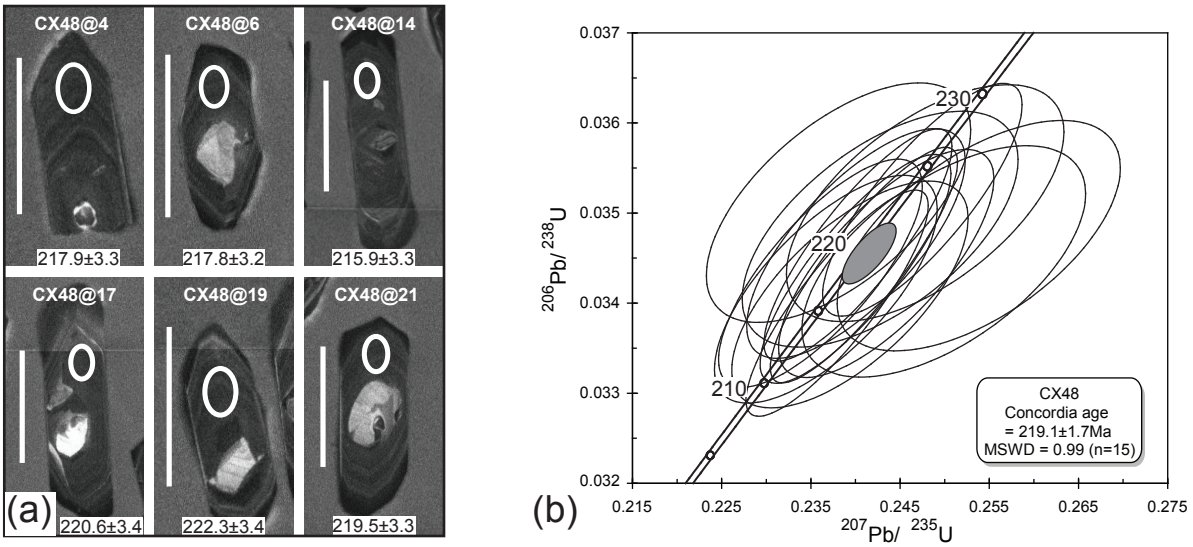
CX48@4
217.9±3.3
CX48@6
217.8±3.2
CX48@14
215.9±3.3
CX48@17
220.6±3.4
CX48@19
222.3±3.4
CX48@21
219.5±3.3
(a)
(b)
0.037
0.036
0.035
0.034
0.033
0.032
206Pb/238U
0.215
0.225
0.235
0.245
0.255
0.265
0.275
207Pb/ 235U
230
220
210
CX48
Concordia age
= 219.1±1.7Ma
MSWD = 0.99 (n=15)

Figure 12

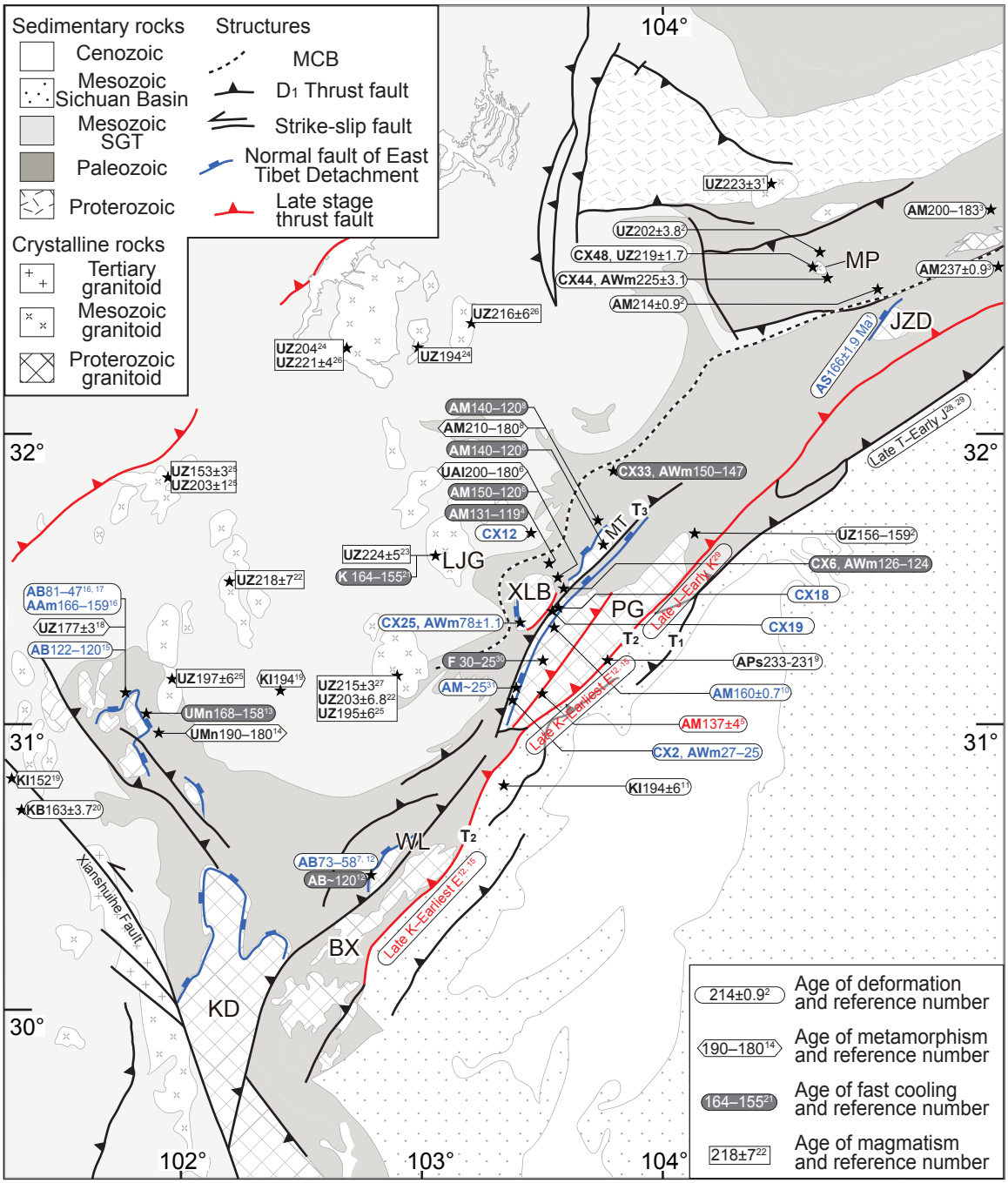
Sedimentary rocks
Cenozoic
Mesozoic Sichuan Basin
Mesozoic SGT
Paleozoic
Proterozoic
Crystalline rocks
Tertiary granitoid
Mesozoic granitoid
Proterozoic granitoid
Structures
MCB
D1 Thrust fault
Strike-slip fault
Normal fault of East Tibet Detachment
Late stage thrust fault
104°
32°
31°
30°
102°
103°
MP
JZD
XLB
PG
LJG
MT
WL
BX
KD
Xianshuihe Fault
Late T–Early J
Late J–Early K
Late K–Earliest E
T1
T2
T3
UZ223±3
AM200–183
UZ202±3.8
CX48, UZ219±1.7
CX44, AWm225±3.1
AM214±0.9
AM237±0.9
AS166±1.9 Ma
UZ216±6
UZ204
UZ221±4
UZ194
AM140–120
AM210–180
AM140–120
UAl200–180
AM150–120
AM131–119
CX12
CX33, AWm150–147
UZ153±3
UZ203±1
UZ224±5
K 164–155
UZ218±7
UZ156–159
CX6, AWm126–124
CX18
CX19
APs233-231
AM160±0.7
AM137±4
CX2, AWm27–25
KI194±6
AB81–47
AAm166–159
UZ177±3
AB122–120
CX25, AWm78±1.1
F 30–25
AM~25
UZ215±3
UZ203±6.8
UZ195±6
UZ197±6
KI194
UMn168–158
UMn190–180
KI152
KB163±3.7
AB73–58
AB~120
214±0.9 Age of deformation and reference number
190–180 Age of metamorphism and reference number
164–155 Age of fast cooling and reference number
218±7 Age of magmatism and reference number

Figure 13

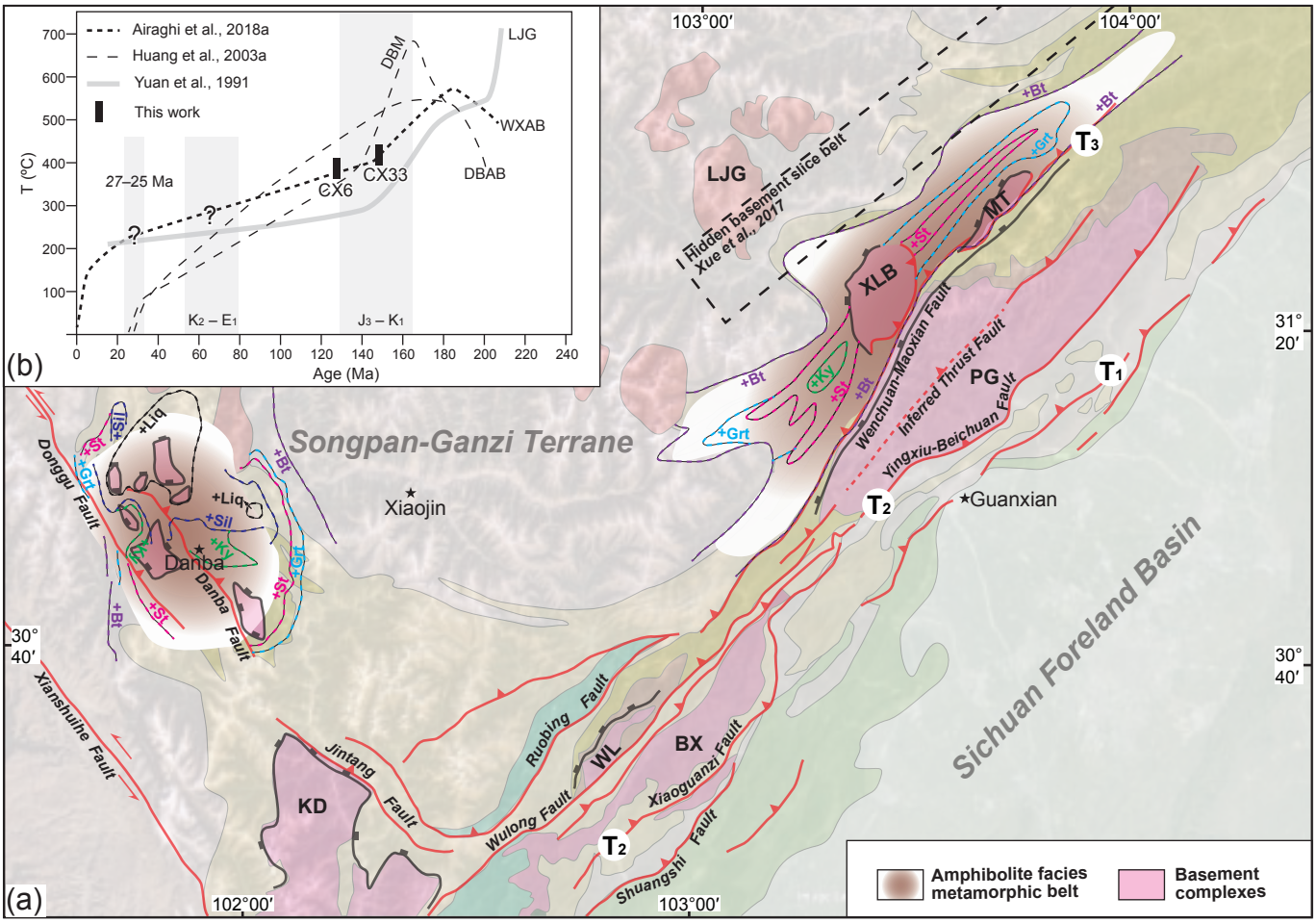
(b)
Airaghi et al., 2018a
Huang et al., 2003a
Yuan et al., 1991
This work
T (°C)
Age (Ma)
27–25 Ma
CX6
CX33
DBM
LJG
WXAB
DBAB
K2 – E1
J3 – K1
(a)
103°00′
104°00′
102°00′
31° 20′
30° 40′
LJG
Hidden basement slice belt
Xue et al., 2017
XLB
MT
PG
T3
T2
T1
Songpan-Ganzi Terrane
Xiaojin
Guanxian
Danba
Danba Fault
Donggu Fault
Xianshuihe Fault
Jintang Fault
KD
Ruobing Fault
WL
BX
Xiaoguanzi Fault
Wulong Fault
Shuangshi Fault
Wenchuan-Maoxian Fault
Inferred Thrust Fault
Yingxiu-Beichuan Fault
Sichuan Foreland Basin
Amphibolite facies metamorphic belt
Basement complexes

Figure 14

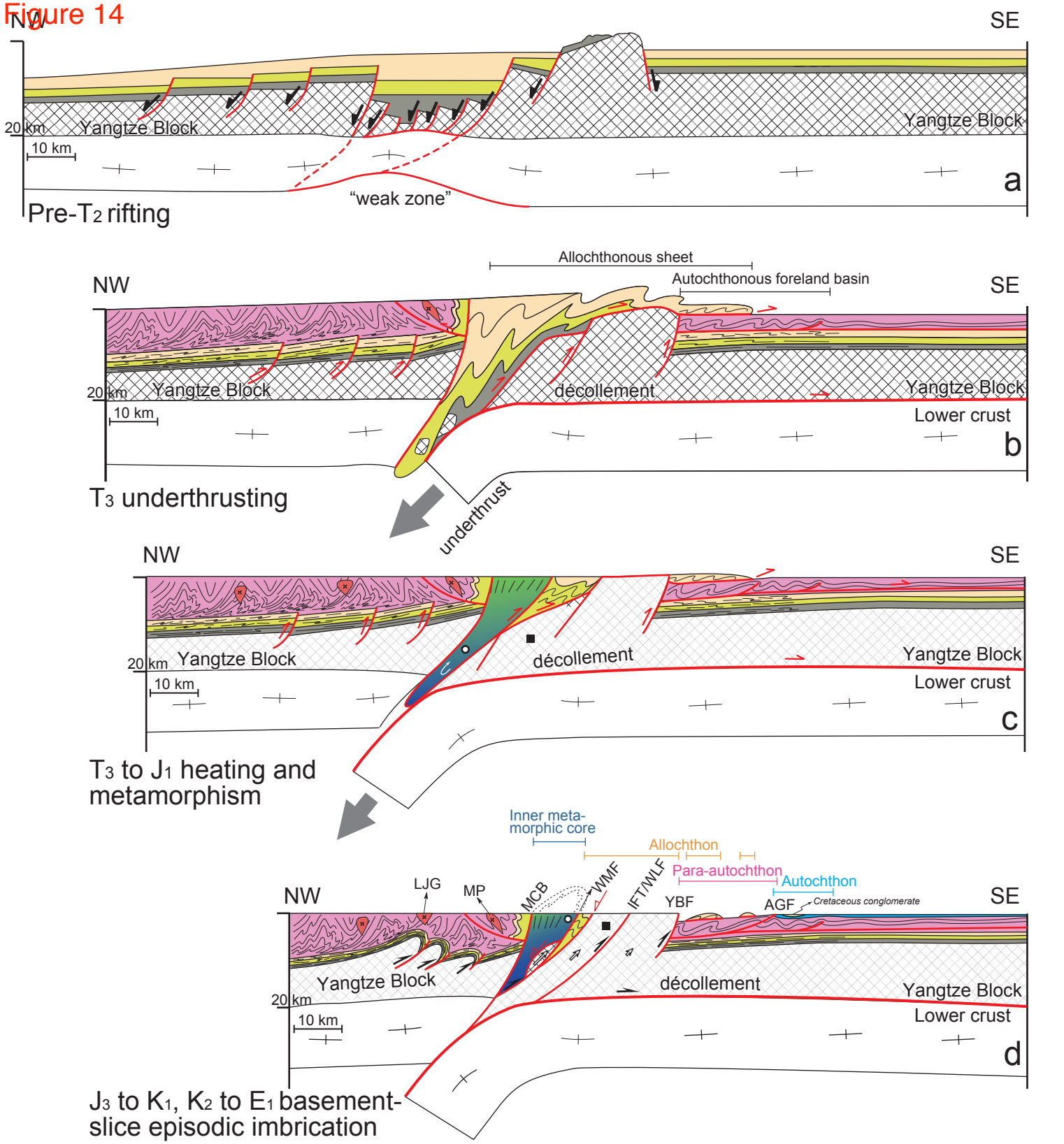
NW
SE
20 km
10 km
Yangtze Block
Yangtze Block
a
Pre-T2 rifting
"weak zone"
Allochthonous sheet
Autochthonous foreland basin
NW
SE
20 km
10 km
Yangtze Block
décollement
Yangtze Block
Lower crust
b
T3 underthrusting
underthrust
NW
SE
20 km
10 km
Yangtze Block
décollement
Yangtze Block
Lower crust
c
T3 to J1 heating and metamorphism
Inner meta-morphic core
Allochthon
Para-autochthon
Autochthon
LJG
MP
MCB
WMF
IFT/WLF
YBF
AGF
Cretaceous conglomerate
NW
SE
Yangtze Block
20 km
10 km
décollement
Yangtze Block
Lower crust
d
J3 to K1, K2 to E1 basement-slice episodic imbrication
Pre T2 normal fault
Reverse fault during T3–aJ1
Episodic and synchronous NW-normal faulting and SE-thrusting during J3–K1, K2–E1
J–Q
T3
D–T2
Є–S
Pt
basement
Meta-unit

Zhenhua Xue, Wei Lin, Yang Chu, Michel Faure, Yan Chen, Wenbin Ji, and Huaning Qiu, 2021, An intracontinental orogen exhumed by basement-slice imbrication in the Longmenshan Thrust Belt of the Eastern Tibetan Plateau: GSA Bulletin, https://doi.org/10.1130/B35826.1.

Supplemental Material

Figure S1. (a) Reflection image show location of the crack in feldspar, same crack in lower middle of Figure 8e from the Mupi pluton. (b) Same crack in Figure a, cross-polarized light. (c) Back scattered electron image show points selected for energy–dispersive X-ray spectrometer measurement. (d and h) Energy–dispersive X-ray spectra of point 1 and point 6 in the crack show typical feature of quartz. (e–g) Energy dispersive X-ray spectra of point 2, point 3, and point 5 indicate component of feldspar with different Ca content.

Figures S2. Features of the samples selected for ^{40}Ar-^{39}Ar dating. Shear plane is defined by fine-grained white mica (c–d) or white mica (a–b, e–f, and g). (h) Field observation of sample CX6, where sigma-shaped quartz lens indicate a top-to-the-SE thrusting. Mineral abbreviations after Kretz (1983). CPL—cross-polarized light; PPL—plain-polarized light.

Figure S3. All samples show high radiogenic ^{40}Ar (Table S2) and almost all steps are clustered at the $^{39}Ar/^{40}Ar$ axis that do not define a real inverse isochron line. The initial $^{40}Ar/^{36}Ar$ ratio originate from the inverse isochron line is meaningless as well. Most of the step-ages calculated both by using initial $^{40}Ar/^{36}$ of 298.56 (Lee et al., 2006) and from the "inverse isochron", show nearly no differences (Table S2). Thus, the inverse isochron ages, though identical to their weighted mean ages or plateau ages, are meaningless and have not been discussed in the main text.

Table S1. Detailed SIMS U-Pb zircon results of sample CX48

Table S2. $^{40}Ar/^{39}Ar$ VG3600 Furnace Step-Heating analytical results

Figure S1

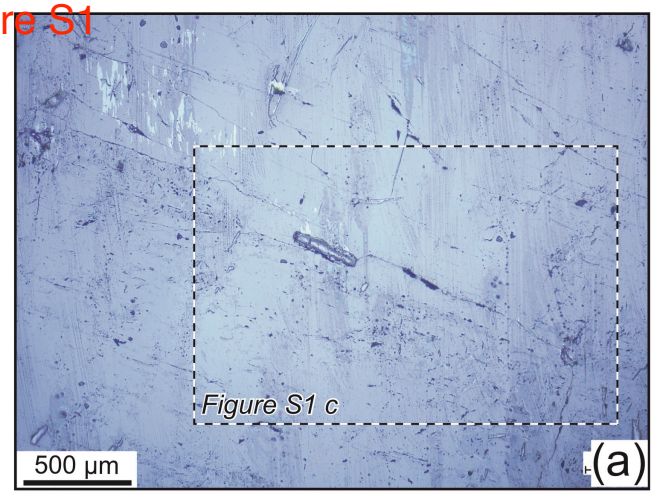
Figure S1 c
500 µm
(a)

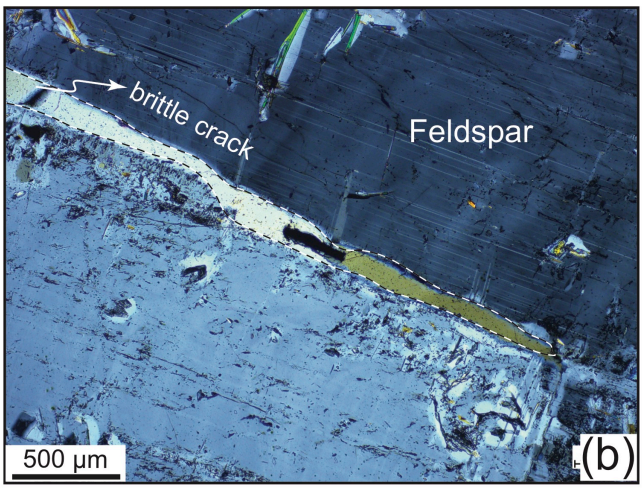
brittle crack
Feldspar
500 µm
(b)

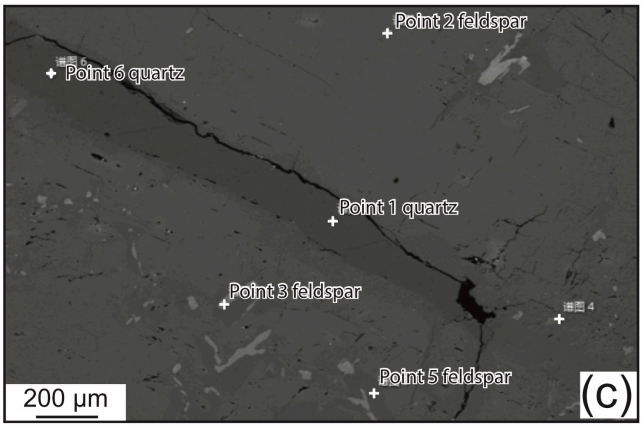
Point 2 feldspar
Point 6 quartz
Point 1 quartz
Point 3 feldspar
Point 5 feldspar
200 µm
(c)

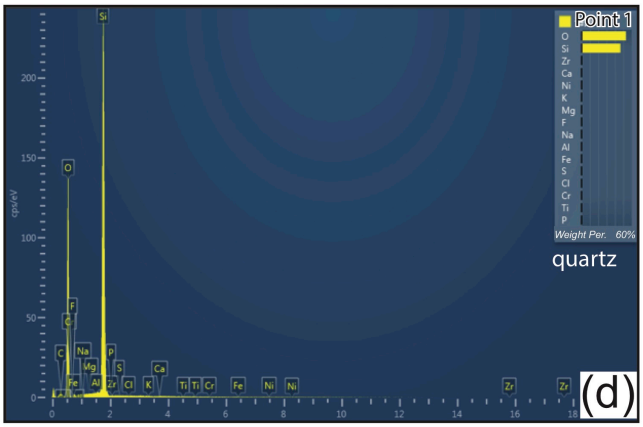
Point 1
quartz
(d)

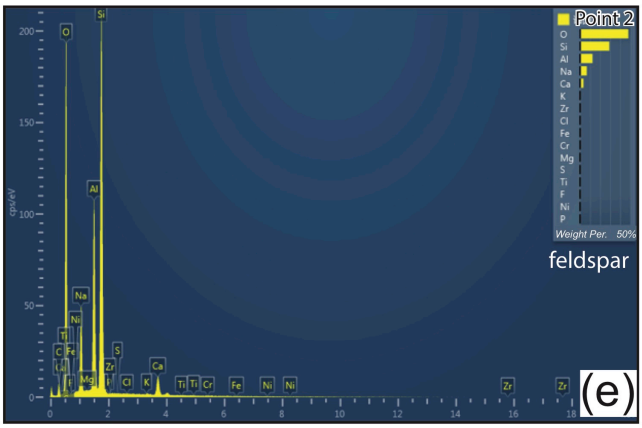
Point 2
feldspar
(e)

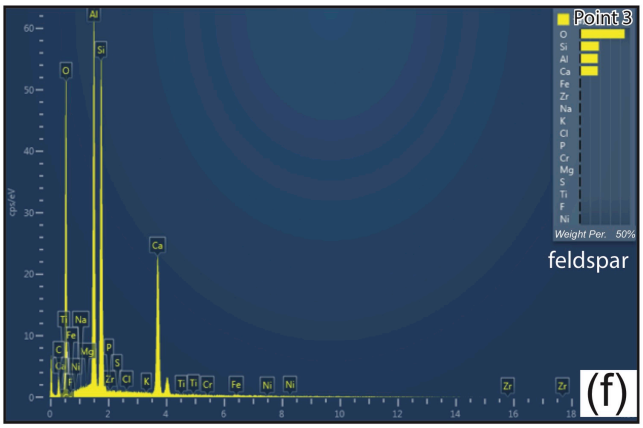
Point 3
feldspar
(f)

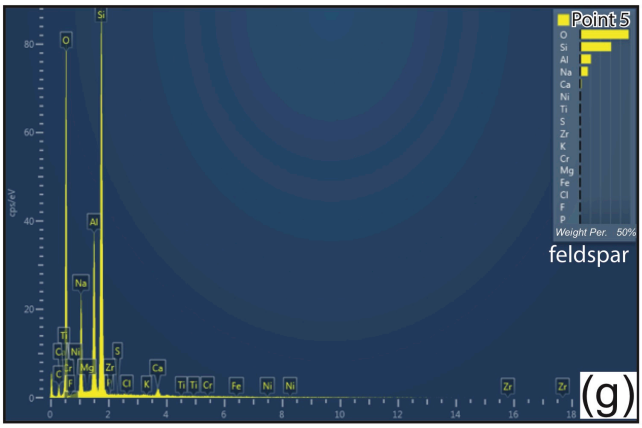
Point 5
feldspar
(g)

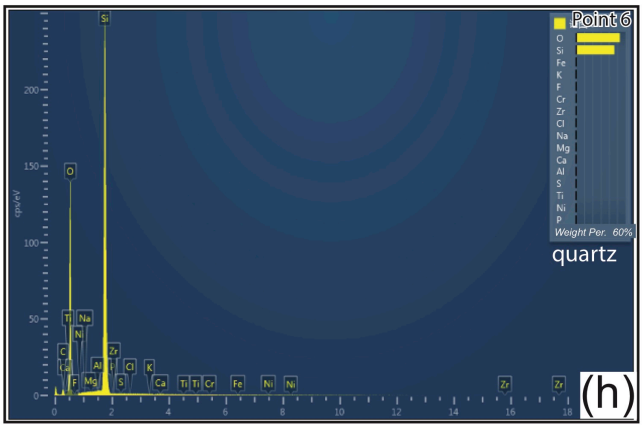
Point 6
quartz
(h)

Figure S2

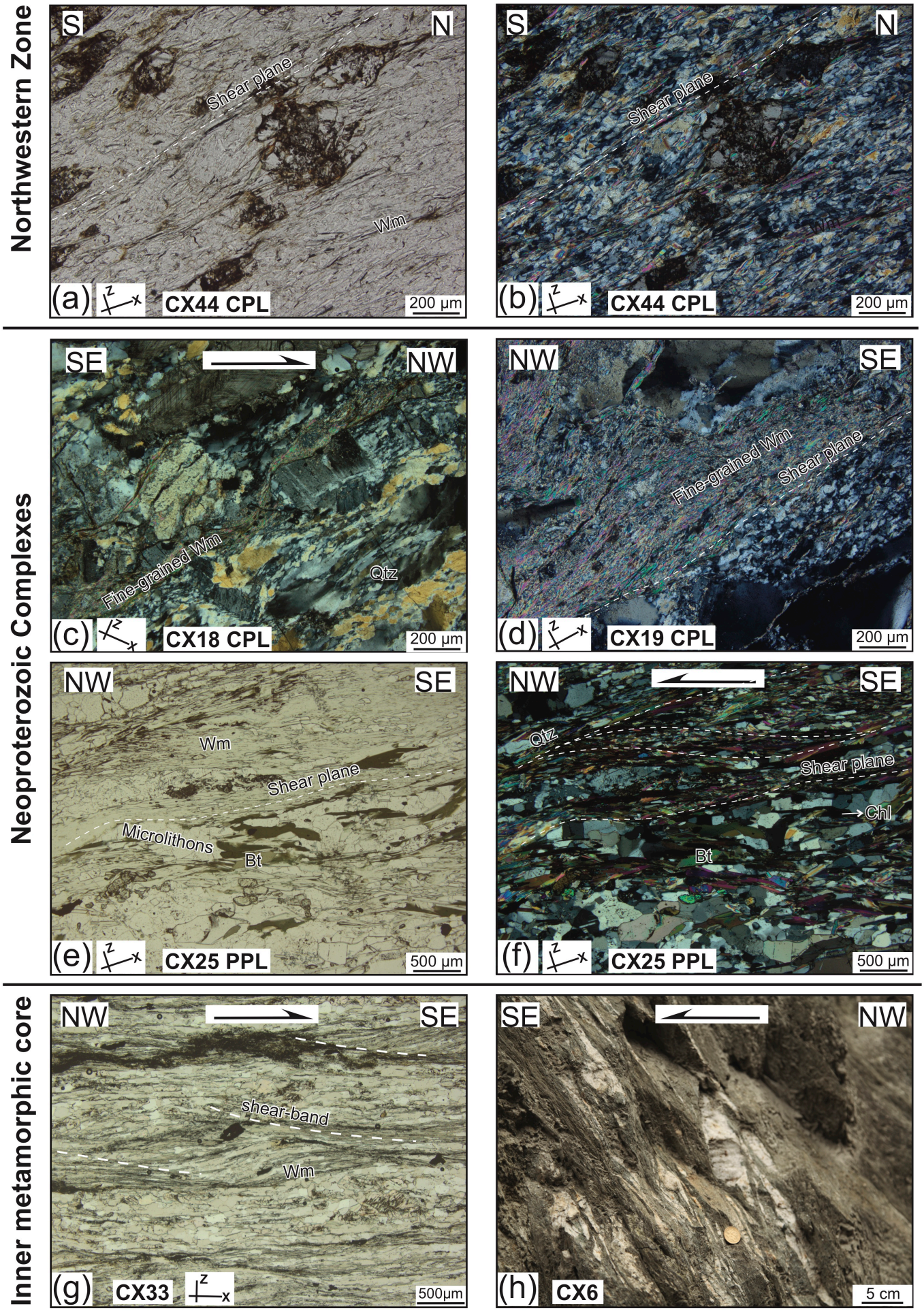
Northwestern Zone
Neoproterozoic Complexes
Inner metamorphic core
S
N
Shear plane
Wm
(a)
CX44 CPL
200 μm
S
N
Shear plane
Wm
(b)
CX44 CPL
200 μm
SE
NW
Fine-grained Wm
Qtz
(c)
CX18 CPL
200 μm
NW
SE
Fine-grained Wm
Shear plane
(d)
CX19 CPL
200 μm
NW
SE
Wm
Shear plane
Microlithons
Bt
(e)
CX25 PPL
500 μm
NW
SE
Qtz
Shear plane
Chl
Bt
(f)
CX25 PPL
500 μm
NW
SE
shear-band
Wm
(g)
CX33
500μm
SE
NW
(h)
CX6
5 cm

Figure S3

Northwestern Zone

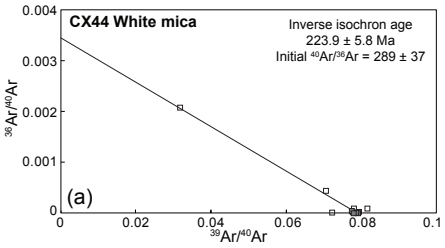

Southeastern Zone -- *Inner metamorphic core*

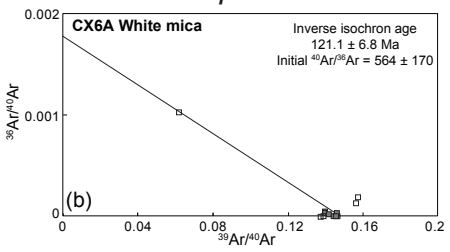

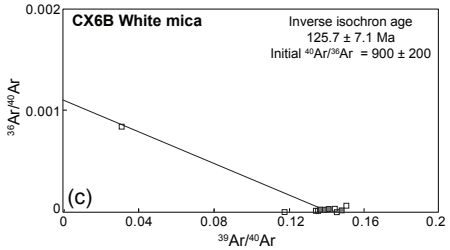

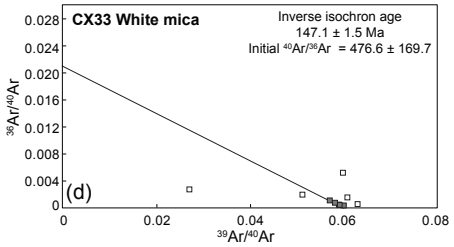

Basement Complex